



# Regimes in the axisymmetric stiction of thin elastic plates

Hang Li, Chuanli Yu, Zhaohe Dai \*

Department of Mechanics and Engineering Science, State Key Laboratory for Turbulence and Complex Systems, College of Engineering, Peking University, Beijing 100871, China

## ARTICLE INFO

### Keywords:

Adhesion  
Stiction  
Thin plates  
2D materials  
MEMS  
Reliability analysis

## ABSTRACT

This work considers the adhesion of a thin, prestressed elastic plate to the bottom of a microcavity – a scenario that can be found frequently in thin-film devices from pressure sensors to microfluidics. This adhesion phenomenon is also referred to as stiction in the field of nano/microelectromechanical systems (N/MEMS); the geometry we consider is axisymmetric (thereby we term this problem *axisymmetric stiction*). Motivated by the extreme thinness of increasingly exploited nanofilms such as 2D materials in functional devices, various limiting regimes of the axisymmetric stiction problem that arise due to the interplay of the bending, stretching, and pretension effects are discussed. Specifically, key dimensionless physical parameters in this problem are discussed and the range of these parameters for the classification of different regimes is outlined. This classification allows for analytical/asymptotic solutions for the critical adhesion conditions and the adhesion length in different regimes, many of which are not yet available in the literature. These analytical results are verified numerically and also compared with experiments based on 3–500 nm thick 2D materials. As such, this work provides a complete overview of the physically relevant regimes associated with axisymmetric stiction, establishing a regime diagram that can be directed used for the evaluation of the structural reliability of rapidly emerging thin plate devices.

## 1. Introduction

Thin plates serve as fundamental components in a diverse array of natural and engineered systems, encompassing bio-tissues, wearable electronics, 2D materials, and M/NMES [1]. In these systems, the adhesion effect emerges as a crucial consideration in the fabrication, manipulation, and functionality of plates, especially at small scales [2]. An illustrative example arises when a thin plate suspends over a shallow cavity (Fig. 1), subjected to intermolecular forces emanating from the cavity. This configuration frequently manifests in N/MEMS devices, such as pressure sensors [3–6], field-effect transistors [7], and recently, nanocapillaries [8]. The presence of intermolecular forces can induce the plate to sag or even adhere to the base of the cavity, presenting both benefits and burdens in the design of thin plate based functional devices.

On the one hand, adhesion between a thin plate and its substrate has long been considered a potential failure mechanism, known as stiction, particularly in the field of N/MEMS [1,9]. Extensive efforts have been dedicated to understanding and circumventing this problem. For example, in the gas impermeability tests in Sun et al. [10], testing a thin layer, such as graphene, requires sealing a cavity (Fig. 1a). To enhance testing sensitivity, it becomes imperative not only to reduce the cavity volume but also to ensure a sufficiently large cavity depth

to prevent adhesion of the layer to the cavity. Similarly, in the design of nanochannels used to investigate nanoscale capillary condensation, meticulous attention has been paid to setting the thickness of the top plate to be large enough (e.g. 50–70 nm) to avert the collapse of the nanochannel [8]. More frequently, in scenarios where ultra-thin 2D materials are used for sensitive pressure sensors [3–6,11], drumhead-shaped devices can fail due to stiction of functional plates after prolonged operation (see Fig. 1b), even though such a configuration has survived in the fabrication process [12]. In fact, whether stiction occurs depends on a number of factors, including the size and depth of the cavity, the thickness of the plate, and the interface properties of the system, which have required screening tests before deploying relevant mechanical devices (Fig. 1 c), for example by colorimetry [13]. The issue of adhesion of thin plates also extends to larger scales, as evidenced in wearable electronics (Fig. 1d). In such contexts, remedies such as filling the cavity with incompressible liquids have proven to be helpful [14,15].

On the other hand, the adhesion of thin plates has been intentionally exploited for functionalities. For instance, similar to strain engineering techniques applied in traditional semiconductors [16], 2D material transistors have been affixed onto trench-like structures to induce

\* Corresponding author.

E-mail address: [daizh@pku.edu.cn](mailto:daizh@pku.edu.cn) (Z. Dai).

<https://doi.org/10.1016/j.ijmecsci.2024.109740>

Received 2 July 2024; Received in revised form 26 August 2024; Accepted 14 September 2024

Available online 19 September 2024

0020-7403/© 2024 Elsevier Ltd. All rights are reserved, including those for text and data mining, AI training, and similar technologies.

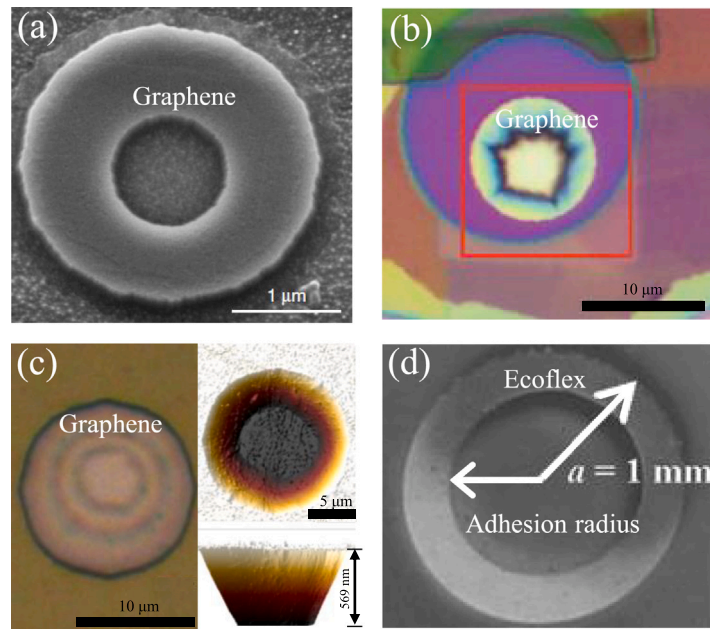


**Fig. 1.** Illustrations depicting various instances of thin plate stiction. (a) Scanning electron microscopy (SEM) image of a graphene layer sealing a microcavity for a gas impermeability test [10]. (b) Optical and atomic force microscopy (AFM) height image showing the collapse of a graphene-based resonant pressure sensor after 2 months of operation [12]. (c) AFM height image displaying a failed graphene mechanical device due to graphene adhering to the bottom of a cavity [13]. (d) Photograph of a skin-mounted device revealing the collapse of the top soft layer onto the cavity [14].

tensile strain within the atomic layer [16]. Such strain manipulation can significantly enhance the carrier mobilities of 2D semiconductors (e.g., up to 152% in Chen et al. [7]). In addition, the “stictioned” configuration has been used to develop the so-called touch model pressure sensors that feature good linearity, large over-range pressure, and robust structure compared to typical “non-stictioned”, suspended pressure sensors [17–22]. Notably, in these instances, the lateral dimension of the plates ranges from a few micrometers to millimeters, and the aspect ratio varies from  $10^1$  to  $10^4$  (see Table 1 for more details).

To either avoid or exploit the adhesion of thin plates, it is crucial to establish formal models capable of predicting both the critical condition for the adhesion to occur and the contact length after the occurrence of the adhesion [2]. This underscores the adhesion problem of thin plates, which we consider in this work, and the term *axisymmetric stiction* given its axisymmetry. From the perspective of adhesion or fracture mechanics, it is obvious that the adhesion energy between solid surfaces is the exclusive source driving the stiction [23]. The complexity of this problem comes from the nonlinear elasticity inherent in thin plates and the intricate interplay of plate bending, transverse-deflection-induced membrane stretching, and initial residual pretension within the plate [24,25]. Previous work has focused mainly on a limiting case of the axisymmetric stiction problem, providing analytical or approximate solutions when one or two of the bending, stretching, and pretension effects are neglected (see Table A.3). For example, various works have offered analytical solutions by linearizing the problem by neglecting the stretching and pretension within the plate [15,26–28]. The nonlinearities that emerge in elasticity and geometry have been carefully addressed by Chandler and Vell [29], but without considering the adhesion effect. To address the adhesion problem with the nonlinearity associated with membrane stretching, some studies have employed numerical approaches [28,30] or derived approximate solutions under the assumption of uniform radial stress [31–33], albeit this assumption lacks physical accuracy. By contrast, Jin [34] studied a similar problem under the condition of controlled loads and provided exact solutions of the force–displacement response of both linearized and nonlinear situations while explicit, analytical results were limited to critical contact radius. Moreover, although the critical adhesion conditions and adhesion behavior of thin plates can be discussed at

various limits, it is not fully clear how these different regimes appear and when they are applicable. Consequently, a regime diagram that can provide direct guidelines for either avoiding or exploiting the stiction in experiments remains lacking.

Here, a unified diagram for different regimes of axisymmetric stiction is presented via combined theories and experiments. The results include some perturbation solutions for stretching-absent and stretching-dominated regimes that were not considered or not properly addressed in previous work. As such, a regime diagram is provided and further verified by controlled experiments involving 3–500 nm thick 2D material plates. This paper is organized as follows. In Section 2, the physical model of axisymmetric stiction is introduced by discussing the nonlinear governing equations. The essential boundary conditions to solve this adhesion problem are also discussed. We identify a few key physical parameters in this problem and investigate potential simplifications of the governing equations under various parameter regimes. The focus of Section 3 will be on four regimes: bending only regime, bending and pretension regime, pretension only regime, and stretching only regime. Within each regime, we present analytical solutions for both the critical adhesion condition and the adhesion length, subsequently verifying these solutions by comparing them to numerical calculations of the un-simplified version of the governing equations. With these results, we construct the regime diagram to elucidate the rich adhesion behaviors of thin plates in the axisymmetric stiction problem in Section 4. We also demonstrate how this diagram can be used for the examination of the structural reliability of relevant thin plate devices in experiments. Finally, we conclude with a summary of the main findings in Section 5.

## 2. The model

### 2.1. Axisymmetric stiction

As depicted in Fig. 2, axisymmetric stiction in a typical device commonly involves a slender plate of thickness  $t$ , suspended above a circular cavity characterized by radius  $R_f$  and depth  $h$ . In typical experimental setups, achieving this configuration often involves placing the thin plate on top of the cavity, which can cause residual stress

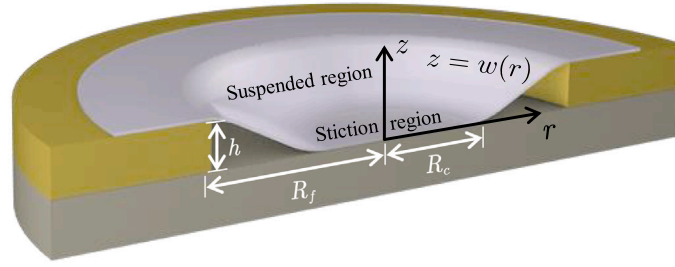


**Fig. 2.** Schematic illustration and notation for the analysis of adhesion of axisymmetric plates. The plate of thickness  $t$  adheres to the bottom of a cavity with an adhesion radius  $R_c$ . The circular cavity is defined by radius  $R_f$  and depth  $h$ .

**Table 1**

Summary of geometrical and controlling parameters of relevant devices in the literature. Note that we have estimated the pretension via a residual strain  $\lesssim 0.1\%$  since it often lies in this range yet precise measurements are usually challenging [1]. Regarding the samples in José Cartamil-Bueno et al. [13], we only list two representative sets of data here.

Reference		Radius $R_f$	Height $h$	Thickness $t$	$\mathcal{K}_h$	$\mathcal{N}$
[14]	S1	$\sim 500 \mu\text{m}$	$\sim 100 \mu\text{m}$	$\sim 200 \mu\text{m}$	$\sim 10^0$	$\lesssim 0.03$
	S2	$\sim 1000 \mu\text{m}$	$\sim 100 \mu\text{m}$	$\sim 200 \mu\text{m}$	$\sim 10^0$	$\lesssim 0.10$
	S3	$\sim 1000 \mu\text{m}$	$\sim 200 \mu\text{m}$	$\sim 200 \mu\text{m}$	$\sim 10^1$	$\lesssim 0.03$
	S4	$\sim 2000 \mu\text{m}$	$\sim 200 \mu\text{m}$	$\sim 200 \mu\text{m}$	$\sim 10^1$	$\lesssim 0.10$
[42]	S5	$\sim 65 \text{ nm}$	$\sim 1 \text{ nm}$	$\sim 52 \text{ nm}$	$\sim 10^{-1}$	$\lesssim 5.20$
	S6	$\sim 65 \text{ nm}$	$\sim 1 \text{ nm}$	$\sim 12 \text{ nm}$	$\sim 10^0$	$\lesssim 5.20$
[10]	S7	$\sim 500 \text{ nm}$	$\sim 50 \text{ nm}$	$\sim 0.34 \text{ nm}$	$\sim 10^5$	$\lesssim 0.10$
	S8	$\gtrsim 1000 \text{ nm}$	$\sim 50 \text{ nm}$	$\sim 0.34 \text{ nm}$	$\sim 10^5$	$\lesssim 0.40$
[13]	S9	$\lesssim 5000 \text{ nm}$	$\sim 630 \text{ nm}$	$\sim 0.68 \text{ nm}$	$\sim 10^7$	$\lesssim 0.06$
	S10	$\gtrsim 5000 \text{ nm}$	$\sim 285 \text{ nm}$	$\sim 0.34 \text{ nm}$	$\sim 10^7$	$\lesssim 0.30$
[43]	S11	$\sim 1500 \text{ nm}$	$\sim 45 \text{ nm}$	$\sim 48 \text{ nm}$	$\sim 10^{-1}$	$\lesssim 1.10$
[8]	S12	$\sim 75 \text{ nm}$	$\sim 1 \text{ nm}$	$\sim 50 \text{ nm}$	$\sim 10^{-2}$	$\lesssim 12.20$
[44]	S13	$\sim 65 \text{ nm}$	$\sim 1 \text{ nm}$	$\sim 70 \text{ nm}$	$\sim 10^{-2}$	$\lesssim 9.40$
[12]	S14	$\sim 5000 \text{ nm}$	$\sim 285 \text{ nm}$	$\sim 7 \text{ nm}$	$\sim 10^4$	$\lesssim 0.30$
[11]	S15	$\sim 2500 \text{ nm}$	$\sim 110 \text{ nm}$	$\sim 6 \text{ nm}$	$\sim 10^5$	$\lesssim 0.52$

or pretension  $N_0$  within the plate [16,35]. For simplicity, we assume this pretension to be uniformly distributed. Additionally, we consider a clamped boundary condition at the edge of the suspended plate at this moment, where it makes contact with the substrate. This condition is equivalent to enforcing an initial constant displacement at the edge of the suspended plate. The geometrical parameters in many experiments satisfy  $t \ll R_f$  and  $h^2/R_f^2 \ll 1$ . We then adopt Föppl–von Kármán (FvK) equations to describe the deflections of the plate [24]. In this context, the mechanical properties of the plate are given by a constant Poisson ratio  $\nu$ , bending stiffness  $B$ , and in-plane stiffness  $Et$ , where  $E$  is Young's modulus [36–38].

When stiction occurs, the plate adheres to the bottom of the cavity, resulting in the formation of a circular contact region of radius  $R_c$  (see Fig. 2). Determining this  $R_c$  necessitates an interfacial law for the interaction between the plate and the substrate [39]. Considering that the depth of the cavity varies from tens of nanometers to a few millimeters, as indicated in the examples discussed in Fig. 1, it is reasonable to model the interface exclusively by the adhesion energy per unit area, denoted  $\gamma$  [40]. This simplification neglects the long-range aspect of intermolecular forces [39,41]. Furthermore, we deliberately neglect the influence of friction between the plate and the substrate. However, this is justifiable in the context of 2D material systems due to the lubricated nature of the surface of the plates [35].

## 2.2. Important parameters

The primary objective of this study is to investigate the potential occurrence of stiction and to analyze how the value of  $R_c$  is affected by the geometric and physical parameters of the system. To facilitate

this, we introduce several dimensionless parameters, which will be extensively discussed later in this work:

$$\lambda = \frac{R_c}{R_f}, \quad \mathcal{N} = \frac{N_0 R_f^2}{Et h^2}, \quad \Gamma = \frac{\gamma R_f^4}{Et h^4}, \quad \mathcal{K}_h = \frac{Et h^2}{B}. \quad (2.1)$$

Here,  $\lambda$  defines the radius of the contact region relative to the radius of the cavity.  $\mathcal{N}$  compares the pretension with the tension induced by deflection, since the plate adhering to the bottom of the cavity would produce a tensile strain  $\epsilon_{\text{induced}} \sim h^2/R_f^2$ .  $\Gamma$  compares the adhesion energy per area with the induced stretching energy density ( $\sim Et \epsilon_{\text{induced}}^2$ ) if stiction occurs. Finally,  $\mathcal{K}_h$  compared the induced stretching energy density to the induced bending energy density ( $\sim B \kappa_{\text{induced}}^2$ ), where the induced curvature  $\kappa_{\text{induced}}$  scales as  $h/R_f^2$ . In Table 1, we summarize these parameters in previous experiments that include wearable electronics, 2D material devices, and other relevant M/NMES. We take  $0.1\%$  as the maximum residual strain for estimation here [1], so  $\mathcal{N}$  is usually found to be less than 10. In contrast,  $\mathcal{K}_h$  in these experiments spans a quite wide range from  $10^{-2}$  to  $10^7$ . These values motivate us to understand the  $\lambda - \Gamma$  relation (i.e., the adhesion length-adhesion strength relation) of this system under different regimes of  $\mathcal{N}$  and  $\mathcal{K}_h$ .

## 2.3. Formulation of the problem

We begin by discussing thin plate theories and the adhesion criterion for the axisymmetric stiction problem. The total energy of the system can be written as

$$\Pi = \Pi_B + \Pi_S - \pi R_c^2 \gamma, \quad (2.2)$$

where  $\Pi_B$  and  $\Pi_S$  are the bending energy and stretching energy stored in the plate, respectively. Under the assumptions of linear material law and moderate rotations [24], we can expand these two elastic energy terms as

$$\Pi_B = 2\pi B \int_{R_c}^{R_f} \frac{1}{2} \left( w'^2 + \frac{1}{r^2} w'^2 + \frac{2}{r} \nu w' w'' \right) r dr, \quad (2.3a)$$

and

$$\Pi_S = 2\pi \int_0^{R_f} \left( \frac{1}{2} N_r \epsilon_r + \frac{1}{2} N_\theta \epsilon_\theta \right) r dr. \quad (2.3b)$$

Here,  $w$  denotes the out-of-plane displacement (Fig. 2) and  $x' = dx/dr$ ;  $N_r$  and  $N_\theta$  are the radial and hoop stress resultants, respectively.  $\epsilon_r = (N_r - \nu N_\theta)/Et$  and  $\epsilon_\theta = (N_\theta - \nu N_r)/Et$  are the radial and hoop strain components, respectively. The kinematics of the midsurface of the plate can give  $\epsilon_r = u' + \frac{1}{2} w'^2$  and  $\epsilon_\theta = u/r$ , where  $u$  is the in-plane displacement on the midsurface.

The energy principle, or variational principle, is the most effective approach for solving this problem, as it allows us to derive both the governing equations and the adhesion conditions across different regimes. We apply the variational principle to the total energy  $\Pi(u, w, w', w'')$  given in Eq. (2.2) with a moving boundary (i.e.,  $\delta R_c \neq 0$ ). By setting  $\delta u \neq 0$ , we obtain the in-plane equilibrium equation:

$$\frac{d}{dr} (r N_r) - N_\theta = 0 \quad (2.4)$$

for  $0 < r < R_f$ . Similarly, considering  $\delta w \neq 0$ , we arrive at the out-of-plane equilibrium equation:

$$B\nabla^2\nabla^2 w - N_r\kappa_r - N_\theta\kappa_\theta = 0 \quad (2.5)$$

for  $R_c < r < R_f$ , where  $\kappa_r = d^2w/dr^2$  and  $\kappa_\theta = r^{-1}dw/dr$  are the radial and hoop curvatures, respectively, and the operator  $\nabla^2 f = d^2f/dr^2 + r^{-1}df/dr$ . The equilibrium Eqs. (2.4) and (2.5) are the axisymmetric version of well-known FvK equations [24]. The governing equations can be easily solved for the adhered part of the plate ( $0 < r < R_c$ ) in which  $w = 0$ . According to the continuity conditions that are naturally used during the variation, we obtain the boundary conditions for the suspended part of the plate:

$$w = 0, \quad w' = 0, \quad \text{and} \quad u' = u/r \quad \text{at} \quad r = R_c, \quad (2.6)$$

where the third condition is a result of the equal-biaxial stress state in the adhered region. In addition, we have natural boundary conditions at the edge of the plate/cavity:

$$w = h, \quad w' = 0, \quad \text{and} \quad u/r = (1 - \nu)N_0/Et \quad \text{at} \quad r = R_f, \quad (2.7)$$

where the third condition comes from the prescribed in-plane displacement due to the presence of pretension. Lastly, the consideration of adhesion in the total energy leads to a jump in the curvature of the plate at the edge of the contact region ( $r = R_c$ ):

$$\gamma - \frac{1}{2}B[w''(R_c)]^2 = 0, \quad (2.8)$$

which has also been discussed in Refs. [45–47]. Physically, this condition implies that the energy release rate of the plate at the adhesion front equals the adhesion energy.

It is convenient to introduce the Airy stress function  $\phi$  with  $N_r = r^{-1}d\phi/dr$  and  $N_\theta = d^2\phi/dr^2$  so that the in-plane equilibrium Eq. (2.4) is automatically satisfied. As such, Eq. (2.5) becomes

$$B\nabla^2\nabla^2 w - [\phi, w] = 0, \quad (2.9)$$

and a compatibility condition for the Airy stress function  $\phi$  emerges

$$\nabla^2\nabla^2\phi + \frac{1}{2}Et[w, w] = 0, \quad (2.10)$$

where the operator  $[f, g] = \frac{1}{r} \frac{d}{dr} \left( \frac{df}{dr} \frac{dg}{dr} \right)$ .

#### 2.4. Non-dimensionalization

We choose the radius of the plate  $R_f$  and the depth of the cavity  $h$  as the horizontal and vertical length scale, respectively, along with the intrinsic in-plane stiffness  $Et$ , to re-scale the problem. Specifically, we perform

$$\rho = \frac{r}{R_f}, \quad W = \frac{w}{h}, \quad \bar{u} = \frac{uR_f}{h^2}, \quad \bar{N}_r = \frac{N_r R_f^2}{Eth^2}, \quad \bar{N}_\theta = \frac{N_\theta R_f^2}{Eth^2}, \quad \bar{\Pi} = \frac{\Pi R_f^2}{Eth^4}, \quad \Phi = \frac{\phi}{Eth^2}. \quad (2.11)$$

We then obtain the dimensionless form of the out-of-plane equilibrium equation

$$\mathcal{K}_h^{-1} \frac{d}{d\rho} \left\{ \rho \frac{d}{d\rho} \left[ \frac{1}{\rho} \frac{d}{d\rho} \left( \rho \frac{dW}{d\rho} \right) \right] \right\} - \frac{d}{d\rho} \left( \frac{d\Phi}{d\rho} \frac{dW}{d\rho} \right) = 0 \quad (2.12)$$

and the compatibility equation

$$\rho \frac{d}{d\rho} \left[ \frac{1}{\rho} \frac{d}{d\rho} \left( \rho \frac{d\Phi}{d\rho} \right) \right] + \frac{1}{2} \left( \frac{dW}{d\rho} \right)^2 = 0, \quad (2.13)$$

subject to

$$W(\lambda) = 0, \quad W'(\lambda) = 0, \quad \Phi(\lambda) = 0, \quad \Phi''(\lambda) - \Phi'(\lambda)/\lambda = 0, \quad (2.14)$$

and the adhesion condition

$$W''(\lambda) = (2\Gamma\mathcal{K}_h)^{1/2}, \quad (2.15)$$

where the key parameters including  $\lambda, \mathcal{N}, \Gamma$  and  $\mathcal{K}_h$  have been introduced in Eq. (2.1). Note that the choice of  $\Phi(\lambda)$  can be arbitrary, since only  $\Phi'$  is physically useful. Eqs. (2.12)–(2.15) complete the theory for the problem of axisymmetric stiction. This boundary value problem (BVP) and the unknown  $\lambda$  can be readily solved using regular BVP solvers built-in MATLAB. In the following, we will make some analytical progress as  $\mathcal{K}_h$  and  $\mathcal{N}$  enter a few limiting regimes (we will also show in Section 4 that these results are not that limited when compared with experiments).

### 3. The regimes

#### 3.1. Bending only regime ( $\mathcal{K}_h \ll 1, \mathcal{K}_h\mathcal{N} \ll 1$ )

We first consider a simplified case in which only the bending energy is considered as the elastic strain energy in the total energy of the system. Such case of axisymmetry has been considered in Refs. [15, 26, 28, 30, 34, 48, 49], with analytical solutions provided. Now, Eq. (2.2) becomes

$$\bar{\Pi} = 2\pi\mathcal{K}_h^{-1} \int_{\lambda}^1 \frac{1}{2} \left( W''^2 + \frac{1}{\rho^2} W'^2 + 2\nu \frac{1}{\rho} W' W'' \right) \rho d\rho - \pi\lambda^2\Gamma. \quad (3.1)$$

This bending-only regime requires that the induced bending energy density ( $\sim Bh^2/R_f^4$ ) is much greater than both the induced stretching energy density ( $\sim Eth^4/R_f^4$ ) and the pretension-contributed energy density ( $\sim N_0h^2/R_f^2$ ), i.e.,

$$\mathcal{K}_h \ll 1 \quad \text{and} \quad \mathcal{K}_h\mathcal{N} \ll 1,$$

according to Eq. (2.1). In this context, the governing equation can be simplified as

$$\frac{d}{d\rho} \left\{ \rho \frac{d}{d\rho} \left[ \frac{1}{\rho} \frac{d}{d\rho} \left( \rho \frac{dW}{d\rho} \right) \right] \right\} = 0 \quad (3.2)$$

and its solution is

$$W = \frac{a_1\rho^2 + a_2\rho^2 \log \rho + a_3 \log \rho + a_4}{(\lambda^2 - 1)^2 - (2\lambda \ln \lambda)^2}, \quad (3.3)$$

where  $a_1, a_2, a_3$  and  $a_4$  are integration constants. We apply the boundary conditions specified in Eq. (2.14) to obtain

$$a_1 = 1 - \lambda^2 - 2\lambda^2 \ln \lambda, \quad a_2 = 2(\lambda^2 - 1), \quad a_3 = 4\lambda^2 \ln \lambda, \quad (3.4)$$

$$a_4 = \lambda^2 [\lambda^2 - 1 + 2 \ln \lambda - 4(\ln \lambda)^2],$$

as well as an expression that can be used to determine the adhesion length  $\lambda$

$$\mathcal{K}_h\Gamma = 8 \left[ \frac{1 + 2 \ln \lambda - \lambda^2}{(\lambda^2 - 1)^2 - (2\lambda \ln \lambda)^2} \right]^2. \quad (3.5)$$

This analytical  $\mathcal{K}_h\Gamma - \lambda$  relation is plotted in Fig. 3a (denoted by solid curve), accompanied by the numerical results (denoted by colored markers) of the unsimplified problem discussed in Eqs. (2.12)–(2.15). Evidently, numerical results can converge to Eq. (3.5) as the parameter regime of  $\mathcal{K}_h \ll 1$  and  $\mathcal{K}_h\mathcal{N} \ll 1$  is reached. Fig. 3a also suggests a critical adhesion energy  $\Gamma_{cr}^I$ , below which there is no solution for the adhesion length. We find this critical adhesion energy and its corresponding critical adhesion length to be

$$\Gamma_{cr}^I \approx 157.3 \mathcal{K}_h^{-1} \quad \text{and} \quad \lambda_{cr}^I \approx 0.18, \quad (3.6)$$

where the superscript I denotes solution under the bending-only limit. For  $\Gamma > \Gamma_{cr}^I$ , two adhesion lengths emerge, both satisfying the adhesion boundary condition (3.5) or (2.15). However, only one of them is physical. To illustrate this, we plot the total energy of the system for  $\Gamma = \Gamma_{cr}^I/2$ ,  $\Gamma_{cr}^I$ , and  $2\Gamma_{cr}^I$  in Fig. 3b. At  $\Gamma = \Gamma_{cr}^I/2$ , the total energy increases monotonically with respect to the adhesion length, suggesting  $\lambda = 0$  (that is, that stiction would not occur at all). When  $\Gamma = \Gamma_{cr}^I$ , a local energy minimum emerges at  $\lambda = \lambda_{cr}$  (indicated by the filled marker in



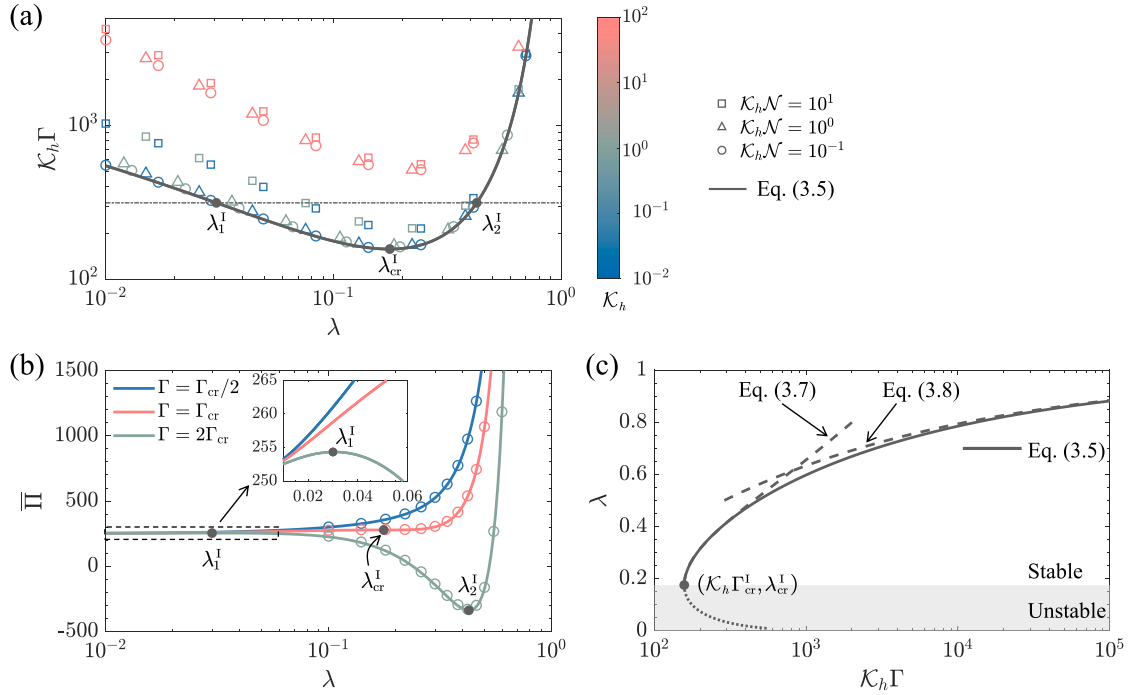


**Fig. 3.** Stiction at the bending-only limit. (a) Adhesion energy  $K_h \Gamma$  as a function of the adhesion length  $\lambda$ . The solid curve is given by Eq. (3.5), while colored markers are given by numerically solving Eqs. (2.12)–(2.15) for various  $K_h \mathcal{N}$  (denoted by different markers) and various  $K_h$  (indicated by the color). (b) The total energy of the system  $\Pi$  as functions of adhesion length  $\lambda$  with three different prescribed adhesion energy  $\Gamma$ . Here we used  $K_h = 10^{-1}$  and  $\mathcal{N} = 0$  for demonstration. The solid curves are calculated analytically by plugging Eq. (3.3) in Eq. (3.1), while the colored markers are numerically computed based on Eq. (2.2). (c) The adhesion length-adhesion strength relation. The solid curve is given by Eq. (3.5) while dashed curves are analytical solutions as  $\Gamma \rightarrow \Gamma_{cr}^I$  (provided in Eq. (3.7)) and  $\Gamma \rightarrow \infty$  (provided in Eq. (3.8)). The filled marker labels the smallest adhesion length that the system can achieve and the minimal adhesion energy that is required for the stiction to take place at the bending-only limit.

Fig. 3b), defining the smallest adhesion length that can be achieved by the system under the bending-only limit. For prescribed  $\Gamma = 2\Gamma_{cr}^I$ , it becomes apparent that the smaller solution (denoted as  $\lambda_1^I$ ) corresponds to a local energy maximum, which is thus unstable. Conversely, the larger solution (say  $\lambda_2^I$ ) represents a stable, local energy minimum. In this scenario, the plate can choose non-stiction (corresponding to the boundary of the energy landscape) or adhere to the cavity bottom with an adhesion length of  $\lambda_2$ , depending on what the initial configuration of the plate is or how carefully this plate is transferred onto the cavity.

It is useful to recapitulate  $\lambda$  as a function of  $\Gamma$  to guide the design of thin plate devices (Fig. 3c). We use a dotted curve to represent the unstable part of the solution and a solid curve for the stable part. In addition, we seek a perturbation solution to Eq. (3.5) by letting  $\Gamma = \Gamma_{cr}^I(1 + \delta_\Gamma)$  and  $\lambda = \lambda_{cr}^I(1 + \delta_\lambda)$  with  $|\delta_\Gamma|, |\delta_\lambda| \ll 1$ , obtaining

$$\lambda \approx \lambda_{cr}^I + 0.11 \left( \sqrt{K_h \Gamma} - \sqrt{K_h \Gamma_{cr}^I} \right)^{1/2} \quad \text{as} \quad \Gamma \rightarrow \Gamma_{cr}^I, \quad (3.7)$$

which gives the dashed curve in Fig. 3c. Similarly, we can obtain the asymptotic behavior as the adhesion force dominates over the elastic force, i.e.,

$$\lambda \sim 1 - (18/K_h \Gamma)^{1/2} \quad \text{as} \quad \Gamma \rightarrow \infty. \quad (3.8)$$

### 3.2. Bending and pretension regime ( $K_h \ll 1$ or $\mathcal{N} \gg 1$ )

We subsequently consider the impact of pretension while still disregarding the influence of the additionally induced tension. This scenario has been investigated in Refs. [34,48,49], yet analytical insights remain elusive thus far. Along the line of the bending-only limit, we may assume  $K_h \ll 1$  and  $K_h \mathcal{N} \sim 1$  for this regime. However, we will soon show that this regime is not limited to  $K_h \mathcal{N} \sim 1$ , particularly given that the (analytical) results in this section can decay to the bending-only limit (already discussed in the preceding section) as  $K_h \mathcal{N} \rightarrow 0$  and to the pretension-only limit (to be discussed in the next section)

as  $K_h \mathcal{N} \rightarrow \infty$ . A more appropriate parameter regime can be given by considering that the induced stretching energy is not important relative to either bending energy or the pretension contributed energy, i.e.,

$$K_h \ll 1 \quad \text{or} \quad \mathcal{N} \gg 1.$$

The total energy in this case can be simplified slightly as

$$\begin{aligned} \Pi = & 2\pi K_h^{-1} \int_{\lambda}^1 \frac{1}{2} \left( W'^2 + \frac{1}{\rho^2} W'^2 + 2\nu \frac{1}{\rho} W' W'' \right) \rho d\rho \\ & + 2\pi \int_0^1 \frac{1}{2} (\mathcal{N} \bar{\epsilon}_r + \mathcal{N} \bar{\epsilon}_\theta) \rho d\rho - \pi \lambda^2 \Gamma. \end{aligned} \quad (3.9)$$

Accordingly, the governing equation can be written as

$$\frac{d}{d\rho} \left\{ \rho \frac{d}{d\rho} \left[ \frac{1}{\rho} \frac{d}{d\rho} \left( \rho \frac{dW}{d\rho} \right) \right] \right\} - K_h \mathcal{N} \frac{d}{d\rho} \left( \rho \frac{dW}{d\rho} \right) = 0. \quad (3.10)$$

The solution of Eq. (3.10) can be identified by acknowledging that it is identical to the solution of  $\nabla^2 W = pW$  if  $p^2 - \eta^2 p = 0$  with  $\eta^2 = K_h \mathcal{N}$ . We then obtain  $p = 0, \eta^2$  and thus

$$W = b_1 I_0(\eta \rho) + b_2 K_0(\eta \rho) + b_3 \log \rho + b_4, \quad (3.11)$$

where  $I_n$  and  $K_n$  ( $n = 0, 1, 2$  to be shortly used) are modified Bessel functions of the first and second kind of order  $n$ , respectively. The integration constants in Eq. (3.11) can be determined using the boundary in Eq. (2.14):

$$\begin{aligned} b_1 &= \frac{\eta [K_1(\eta) - \lambda K_1(\eta \lambda)]}{f(\eta, \lambda)}, \quad b_2 = \frac{\eta [I_1(\eta) - \lambda I_1(\eta \lambda)]}{f(\eta, \lambda)}, \\ b_3 &= \frac{-\eta^2 \lambda [K_1(\eta) I_1(\eta \lambda) - I_1(\eta) K_1(\eta \lambda)]}{f(\eta, \lambda)}, \\ b_4 &= \frac{1 + \eta K_1(\eta) [\eta \lambda I_1(\eta \lambda) \log \lambda - I_0(\eta \lambda)] - \eta I_1(\eta) [\eta \lambda K_1(\eta \lambda) \log \lambda + K_0(\eta \lambda)]}{f(\eta, \lambda)}, \end{aligned} \quad (3.12)$$

where  $f(\eta, \lambda) = 2 + \eta \lambda I_1(\eta \lambda) [\eta K_1(\eta) \log \lambda - K_0(\eta)] - \eta [I_0(\eta \lambda) K_1(\eta) + \lambda I_0(\eta) K_1(\eta \lambda) + I_1(\eta) K_0(\eta \lambda) + \eta \lambda I_1(\eta) K_1(\eta \lambda) \log \lambda]$ . In addition, the use

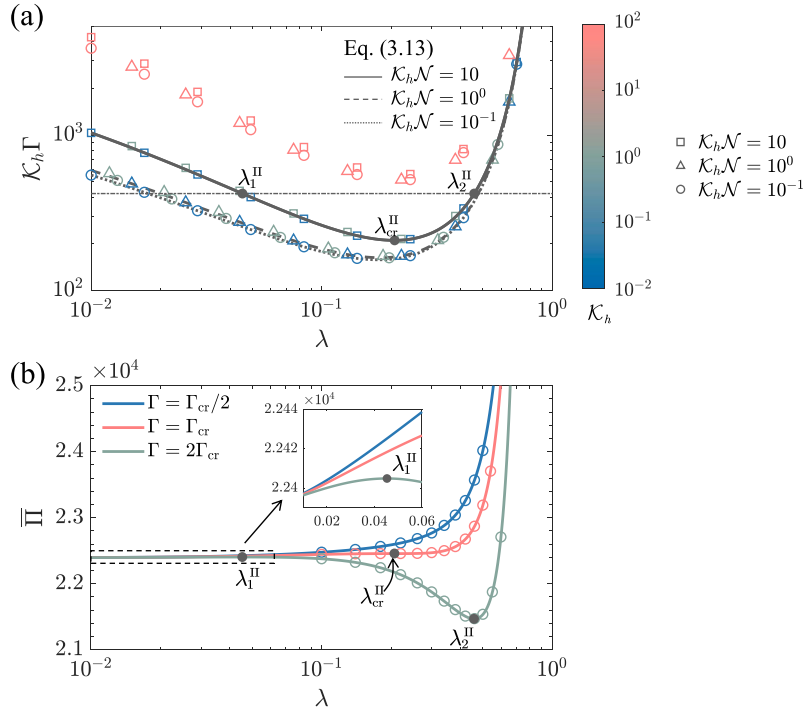


**Fig. 4.** Stiction at the bending and pretension limit. (a) Adhesion energy  $K_h \Gamma$  as functions of adhesion length  $\lambda$  depending on the specific  $K_h \mathcal{N}$ . The curves are given by Eq. (3.13) while the colored markers are calculated based on Eqs. (2.12)–(2.15) for various  $K_h$  and  $\mathcal{N}$ ; (b) Total energy of structure  $\Pi$  as functions of adhesion length  $\lambda$  for various prescribed adhesion energies. Again, solid curves are analytically provided by Eq. (3.9), and the markers are based on unsimplified numerics (here we used  $K_h = 10^{-1}$  and  $K_h \mathcal{N} = 10$  for demonstration).

of the adhesion condition (2.15) can give rise to an expression for the adhesion length:

$$K_h \Gamma = \frac{1}{2} \left\{ \frac{1}{2} b_1 \eta^2 [I_0(\eta\lambda) + I_2(\eta\lambda)] + \frac{1}{2} b_2 \eta^2 [K_0(\eta\lambda) + K_2(\eta\lambda)] - \frac{b_3}{\lambda^2} \right\}^2. \quad (3.13)$$

In Fig. 4a, we plot  $K_h \Gamma$  as a function of  $\lambda$  following Eq. (3.13) for different  $\eta^2 = K_h \mathcal{N}$ . Also included are numerical results of the problem Eqs. (2.12)–(2.15) for various  $K_h$  and  $\mathcal{N}$ . It can be found that Eq. (3.13) is valid for arbitrary  $K_h \mathcal{N}$  as long as  $K_h \ll 1$  or  $\mathcal{N} \gg 1$ . In addition, as  $K_h \mathcal{N} \ll 1$ , Eq. (3.13) approaches a limit that does not depend on  $K_h \mathcal{N}$ , which is the bending-only limit discussed in the preceding subsection. Notably, akin to the stiction behavior observed in the bending-only limit, the regime accounting for both bending and pretension also exhibits a critical adhesion energy/length. Beyond this threshold, a stable adhesion length solution arises. This can be demonstrated by the total energy as a function of  $\lambda$  for different  $\Gamma$  in Fig. 4b, where we used  $K_h = 0.1$  and  $K_h \mathcal{N} = 10$  specifically. Unlike these in the bending-only limit, however, the critical adhesion energy and its associated critical adhesion length in the bending and pretension regime depend on  $K_h \mathcal{N}$ , as shown in Fig. 5.

We further examine the critical adhesion energy and the adhesion length of the system for small and large  $K_h \mathcal{N}$ . For  $K_h \mathcal{N} \ll 1$ , we perform the asymptotic expansion of the right-hand side of Eq. (3.13) up to  $O(\eta^2)$ . Note that the leading-order term of this expansion is found identical to the right-hand side of Eq. (3.5). We therefore seek a perturbation solution of the minimal adhesion length and its critical adhesion energy through  $\lambda_{cr}^{\Pi} = \lambda_{cr}^I + \delta\lambda$  and  $\Gamma_{cr}^{\Pi} = \Gamma_{cr}^I + \delta\Gamma$ . As a result, we obtain the following relations:

$$\lambda_{cr}^{\Pi} \sim \begin{cases} \lambda_{cr}^I + \frac{1}{253} K_h \mathcal{N}, & \text{for } K_h \mathcal{N} \ll 1 \\ \frac{1}{e} - \frac{2+e}{2e} (K_h \mathcal{N})^{-1/2}, & \text{for } K_h \mathcal{N} \gg 1 \end{cases} \quad (3.14)$$

and

$$\Gamma_{cr}^{\Pi} \sim \begin{cases} \Gamma_{cr}^I + 5.5 \mathcal{N}, & \text{for } K_h \mathcal{N} \ll 1 \\ \frac{1}{2} e^2 \mathcal{N} + \frac{2e^2+e^3}{2} \mathcal{N} (K_h \mathcal{N})^{-1/2}, & \text{for } K_h \mathcal{N} \gg 1. \end{cases} \quad (3.15)$$

where  $\lambda_{cr}^I$  and  $\Gamma_{cr}^I$  have been discussed in Eq. (3.6) in the bending-only regime. Similarly, we have included the asymptotic behavior of the critical adhesion energy and adhesion length as  $K_h \mathcal{N} \gg 1$  in Eq. (3.14) and Eq. (3.15). These analytical results agree with Eq. (3.13), as shown in Figs. 4a and b.

### 3.3. Pretension only regime ( $K_h \mathcal{N} \gg 1$ , $\mathcal{N} \gg 1$ )

We then consider a limiting case where the pretension dominates over other effects, including bending and induced stretching of the plate. Continuing with our previous discussion, this simply requires that the energy density associated with pretension ( $\sim N_0 \epsilon_{\text{induced}}$ ) is much higher than both the induced bending energy density ( $\sim B h^2 / R_f^4$ ) and the stretching energy density ( $\sim E h^4 / R_f^4$ ), i.e.,

$$K_h \mathcal{N} \gg 1 \quad \text{and} \quad \mathcal{N} \gg 1.$$

While this specific case has been considered in Refs. [49–54], it is not clear how the critical adhesion condition (2.8) reduces. We address this again by minimizing the total energy, which now reads

$$\bar{\Pi} = 2\pi \int_0^1 \frac{1}{2} (\mathcal{N} \bar{\epsilon}_r + \mathcal{N} \bar{\epsilon}_\theta) \rho \, d\rho - \pi \lambda^2 \Gamma. \quad (3.16)$$

It is found that the governing equation for this form of total energy becomes

$$\nabla^2 W = 0. \quad (3.17)$$

The reduced boundary conditions are  $W(\lambda) = 0$  and  $W(1) = 1$ , yielding solution to Eq. (3.17):

$$W = 1 - \log \rho / \log \lambda. \quad (3.18)$$

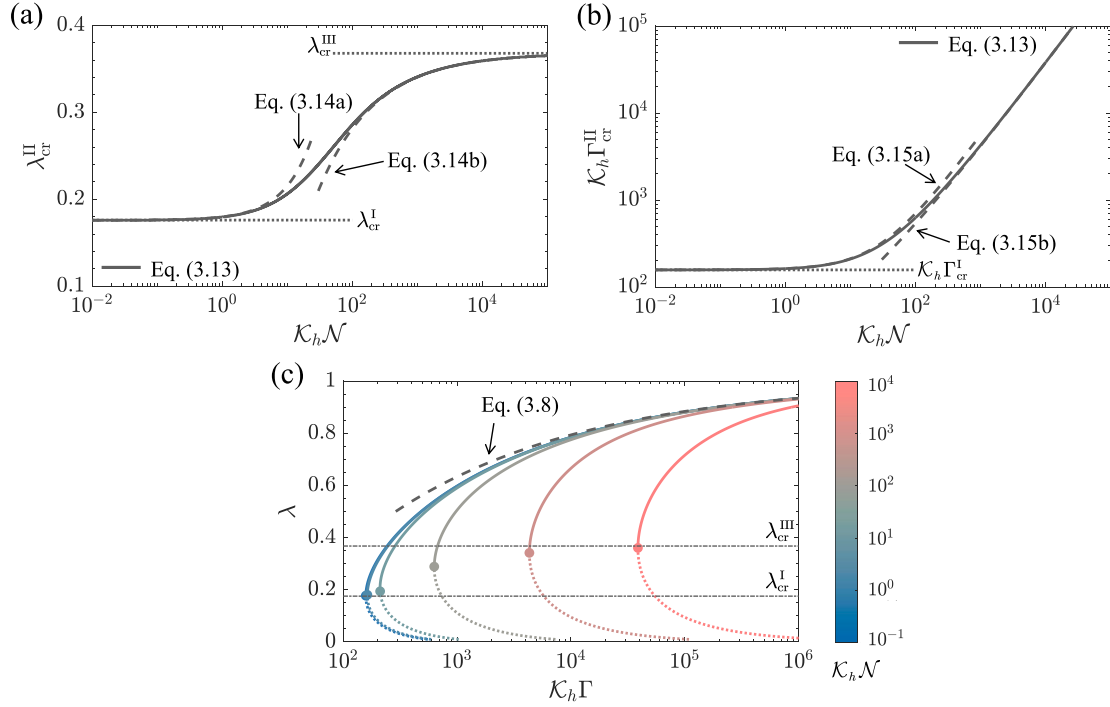


**Fig. 5.** The adhesion length-adhesion strength relation in the bending and pretension limit. (a) The effect of pretension  $K_h N$  on the critical adhesion length  $\lambda_{cr}^{II}$ . The solid curve represents the analytical result as given by Eq. (3.13). The dashed curves are given by the asymptotic solutions in Eq. (3.14) as  $K_h N \ll 1$  and  $K_h N \gg 1$ . The dotted lines represent the critical adhesion length under bending-only ( $\lambda_{cr}^I$ ) and pretension-only regime ( $\lambda_{cr}^{III}$ ); (b) The effect of pretension  $K_h N$  on the critical adhesion energy  $\Gamma_{cr}^{II}$ . The solid curve represents the analytical result as given by Eq. (3.13). The dashed curves are given by Eq. (3.15) as  $K_h N \ll 1$  and  $K_h N \gg 1$  while the dotted line represents the critical adhesion length under bending-only limit given in Eq. (3.6); (c) The relationship between adhesion energy  $\Gamma$  and adhesion length  $\lambda$  for various  $K_h N$  whose values are encoded by the color. The solid curves are given by Eq. (3.13) and the markers label the critical adhesion energy and corresponding adhesion length for various pretension  $K_h N$ .

The order of the governing equation is reduced after dropping the bending term. Accordingly, the adhesion condition is found equivalent to enforcing a kink at  $\rho = \lambda$  with

$$\Gamma = \frac{1}{2} \mathcal{N} [W'(\lambda)]^2. \quad (3.19)$$

With this, we find a simple adhesion strength-adhesion length relation, given by

$$\Gamma = \frac{\mathcal{N}}{2(\lambda \log \lambda)^2}. \quad (3.20)$$

We then plot the  $\Gamma/\mathcal{N} - \lambda$  curve in Fig. 6a (the solid curve) and compare it with the numerical results (colored markers) from the unsimplified model for various  $K_h$  and  $\mathcal{N}$ . It can be found that this pretension-only limit is valid only when  $K_h N \gg 1$  and  $\mathcal{N} \gg 1$  are satisfied. Similarly, there is also a critical adhesion energy  $\Gamma_{cr}^{III}$  and a critical adhesion length in this regime (Fig. 6b), given by

$$\Gamma_{cr}^{III} = \frac{\mathcal{N} e^2}{2} \quad \text{and} \quad \lambda_{cr}^{III} = \frac{1}{e}. \quad (3.21)$$

In addition, we provide the analytical  $\lambda - \Gamma$  relation as the adhesion is close to the critical adhesion energy and approach infinity, i.e.,

$$\lambda = \lambda_{cr}^{III} \left[ 1 + \left( \frac{\Gamma}{\Gamma_{cr}^{III}} - 1 \right)^{1/2} \right] \quad \text{as} \quad \Gamma \rightarrow \Gamma_{cr}^{III}, \quad (3.22)$$

and

$$\lambda = 1 - \left( \frac{\mathcal{N}}{2\Gamma} \right)^{1/2} \quad \text{as} \quad \Gamma \rightarrow \infty, \quad (3.23)$$

which are shown in Fig. 6c as well.

### 3.4. Stretching only regime ( $K_h \gg 1$ , $\mathcal{N} \ll 1$ )

We move on to the last parameter regime of the axisymmetric stiction problem which we term stretching-only regime, i.e.,

$$K_h \gg 1 \quad \text{and} \quad \mathcal{N} \ll 1.$$

This implies that the induced stretching energy density ( $\sim E t h^4 / R_f^4$ ) due to stiction is much greater than both the induced bending energy density ( $\sim B h^2 / R_f^2$ ) and the pretension-associated energy density ( $\sim N_0 h^2 / R_f^2$ ). Then, the total energy of the system reads

$$\bar{H} = 2\pi \int_0^1 \frac{1}{2} (\bar{N}_r \bar{\epsilon}_r + \bar{N}_\theta \bar{\epsilon}_\theta) \rho d\rho - \pi \lambda^2 \Gamma. \quad (3.24)$$

Similarly, variational analysis of the total energy  $\bar{H}$  with a movable boundary at  $\rho = \lambda$  can give governing equations of the problem, including the out-plane equilibrium equation

$$\frac{d}{d\rho} (\Phi' W') = 0, \quad (3.25)$$

and a compatibility equation

$$\rho \frac{d}{d\rho} \left[ \frac{1}{\rho} \frac{d}{d\rho} (\rho \Phi') \right] + \frac{1}{2} W'^2 = 0. \quad (3.26)$$

Here we have adopted the Airy stress function  $\Phi$  for convenience with  $\bar{N}_r = \Phi'/\rho$  and  $\bar{N}_\theta = \Phi''$ . In the stretching-only regime, this problem is to be solved with

$$W(\lambda) = 0, \quad W(1) = 1, \quad (3.27)$$

$$\Phi'(\lambda) - \lambda \Phi''(\lambda) = 0, \quad \Phi''(1) - \nu \Phi'(1) \rightarrow 0,$$

together with the reduced adhesion condition at  $\rho = \lambda$ :

$$\Gamma = \frac{1}{2\lambda} \Phi'(\lambda) [W'(\lambda)]^2. \quad (3.28)$$

Previously analytical solutions to the nonlinear problem specified in Eqs. (3.25) to (3.28) typically involve assumptions such as uniform,

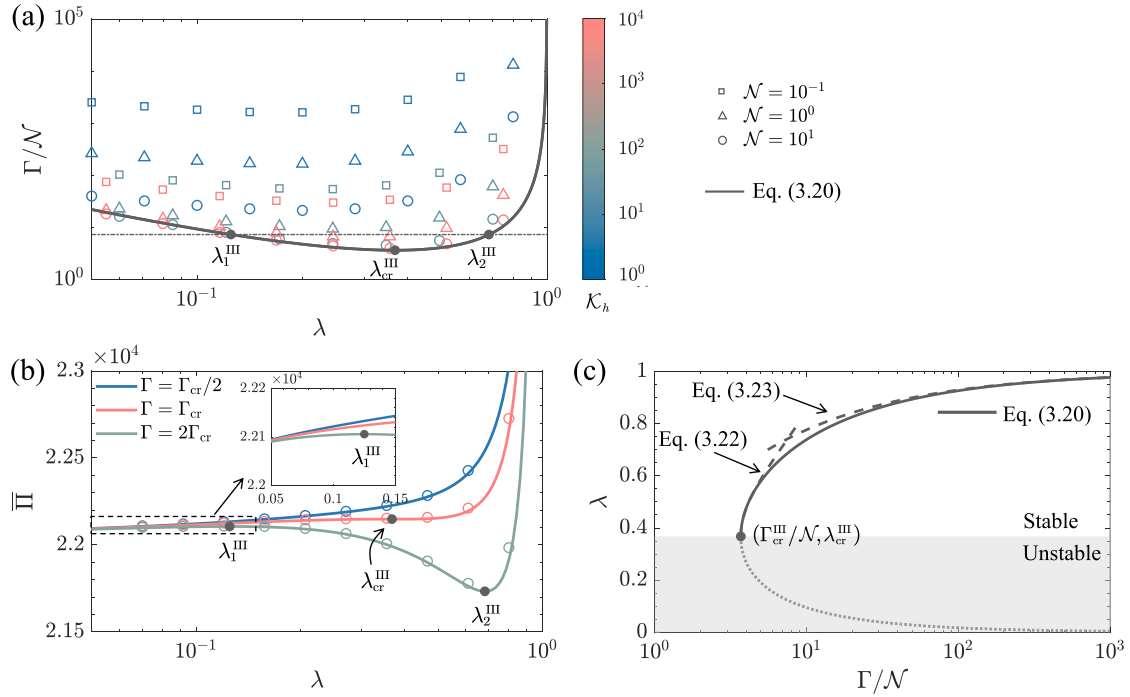


**Fig. 6.** Stiction at the pretension-only limit (in this case the elastic plate behaves like a soap film). (a) The master adhesion strength-adhesion length curve (solid line given by Eq. (3.20)) and its comparison with numerical results (colored markers) for various  $\mathcal{K}_h$  and  $\mathcal{N}$ . (b) The total energy of the system as functions of adhesion length  $\lambda$  for various prescribed adhesion energies. Solid curves denote the total energy calculated using the pretension-only assumption (i.e., Eq. (3.16)) while colored markers are from the un-simplified model using  $\mathcal{K}_h = 10^4$  and  $\mathcal{N} = 10^2$ . (c) Adhesion length as a function of adhesion strength given by Eq. (3.20). The filled marker  $(\Gamma_{cr}^{III}/\mathcal{N}, \lambda_{cr}^{III})$  denotes the smallest stable adhesion length and its corresponding adhesion energy in the pretension-only regime. Dashed curves are perturbation solutions obtained as  $\Gamma \rightarrow \Gamma_{cr}^{III}$  (3.22) and  $\Gamma \rightarrow \infty$  (3.23).

constant stresses [31,32], leading to limited accuracy. Alternatively, the solution given by Jin [34] is exact but implicit, so only  $\lambda_{cr}^{IV} \approx 1.9$  was discussed with other important information such as the missing critical adhesion. Here, we try a Scherwin-type solution [55–57]. The idea is based on the following form of solution

$$\widehat{W}(\rho) = 1 - \frac{1 - \rho^{2/3}}{1 - \lambda^{2/3}} \quad \text{and} \quad \widehat{\Phi}'(\rho) = \frac{\rho^{1/3}}{4(1 - \lambda^{2/3})^2}, \quad (3.29)$$

that can satisfy the governing equation but not boundary conditions. We then consider additional perturbation term

$$W = \widehat{W} + \widetilde{W} \quad \text{and} \quad \Phi' = \widehat{\Phi}' + \widetilde{\Phi}' \quad (3.30)$$

with  $|\widetilde{W}| \ll \widehat{W}$  and  $|\widetilde{\Phi}'| \ll \widehat{\Phi}'$ . Substituting Eq. (3.30) into the equilibrium Eq. (3.25) and the compatibility Eq. (3.26) and neglecting high-order terms, we obtain a pair of simple perturbed governing equations

$$\widetilde{\Phi}' \widehat{W}' + \widetilde{W}' \widehat{\Phi}' = 0, \quad (3.31)$$

and

$$\rho \frac{d}{d\rho} \left[ \frac{1}{\rho} \frac{d}{d\rho} (\rho \widetilde{\Phi}') \right] + \widetilde{W}' \widehat{W}' = 0. \quad (3.32)$$

Combining the two equations can lead to a single, analytically solvable equation for  $\widetilde{\Phi}$ :

$$\rho \frac{d}{d\rho} \left[ \frac{1}{\rho} \frac{d}{d\rho} (\rho \widetilde{\Phi}') \right] - \frac{16}{9\rho} \widetilde{\Phi}' = 0, \quad (3.33)$$

By solving this, we have

$$W(\rho) = 1 - \frac{1}{1 - \lambda^{2/3}} \left[ 1 - \rho^{2/3} + \frac{4}{3}d_1(\rho^2 - 1) - 2d_2(\rho^{-4/3} - 1) \right] \quad (3.34)$$

and

$$\Phi' = \frac{1}{(1 - \lambda^{2/3})^2} \left( \frac{1}{4}\rho^{1/3} + d_1\rho^{5/3} + d_2\rho^{-5/3} \right), \quad (3.35)$$

that can satisfy all equations in (3.25) to (3.27). In particular, integration constants  $d_1$  and  $d_2$  are determined from the boundary conditions in Eq. (3.27):

$$d_1 = \frac{4(1 - 3\nu) + \lambda^2(5 + 3\nu)}{16(3\nu - 5) + 4\lambda^{10/3}(5 + 3\nu)} \quad \text{and} \quad d_2 = \frac{\lambda^2[5 - 3\nu + \lambda^{4/3}(1 - 3\nu)]}{16(3\nu - 5) + 4\lambda^{10/3}(5 + 3\nu)}. \quad (3.36)$$

As a result, we are able to use such perturbation solution and Eq. (3.28) to determine the adhesion length, which satisfies

$$\Gamma = \frac{(\lambda^2 + 4d_1\lambda^{10/3} + 4d_2)(\lambda^2 - 4d_1\lambda^{10/3} - 4d_2)^2}{18\lambda^{22/3}(\lambda^{2/3} - 1)^4}. \quad (3.37)$$

In Fig. 7a, we plot the analytical  $\Gamma$ - $\lambda$  relation in Eq. (3.37), together with the numerical results of Eqs. (2.12)–(2.15) (circles for  $\nu = 1/3$  and triangles for  $\nu = 1/2$ ). We find good agreement between our analytical results and the numerical results, particularly near the point of critical adhesion. Besides, since the effect of Poisson's ratio is limited, we use  $\nu = 1/3$  here to further simplify Eq. (3.37), which can give rise to

$$\lambda \approx \lambda_{cr}^{IV} + 0.14(\Gamma - \Gamma_{cr}^{IV})^{1/2} \quad \text{as} \quad \Gamma \rightarrow \Gamma_{cr}^{IV}, \quad (3.38)$$

and

$$\lambda \approx 1 - \left( \frac{2\Gamma}{9} \right)^{1/3} \quad \text{as} \quad \Gamma \rightarrow \infty, \quad (3.39)$$

where

$$\Gamma_{cr}^{IV} \approx 3.0 \quad \text{and} \quad \lambda_{cr}^{IV} \approx 0.19. \quad (3.40)$$

Note that the value of  $\lambda_{cr}^{IV} \approx 0.19$  is identical to the finding in [34].

#### 4. Comparisons with experiments

##### 4.1. A regime diagram

Having discussed the rich adhesion behavior of the thin elastic plates at various regimes, we then combine these analytical results into



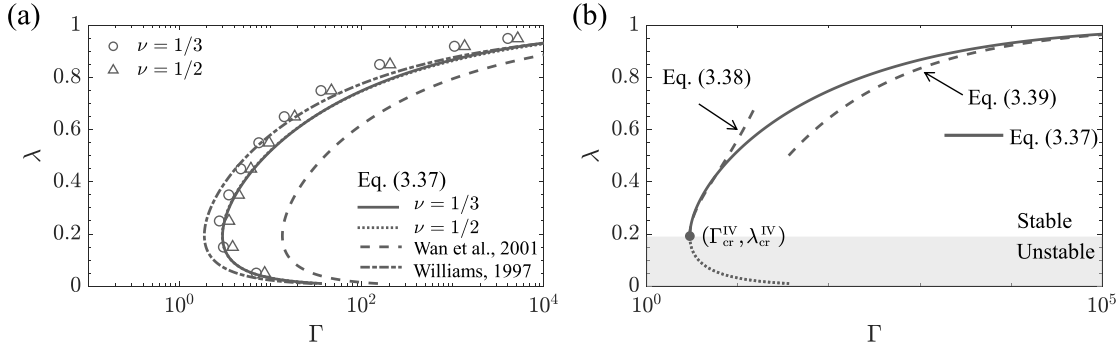


**Fig. 7.** Stiction at the stretching-only limit. (a) The adhesion length-adhesion strength relation provided by various methods, including numerics (markers, using  $\mathcal{K}_h = 10^4$  and  $\mathcal{N} = 0$  for demonstration), the solution by Wan [32], the solution by Williams [31], and our perturbation solution (3.37). Our solution is insensitive to the Poisson's ratio so the solid and dotted curves overlap together. (b) The adhesion length-adhesion strength relation plotted using the perturbation solution with the analytical results as  $\Gamma \rightarrow \Gamma_{cr}^{IV}$  (3.38) and  $\Gamma \rightarrow \infty$  (3.39). The filled marker  $(\Gamma_{cr}^{IV}, \lambda_{cr}^{IV})$  denotes the smallest stable adhesion length and its corresponding adhesion energy in the stretching-only regime.

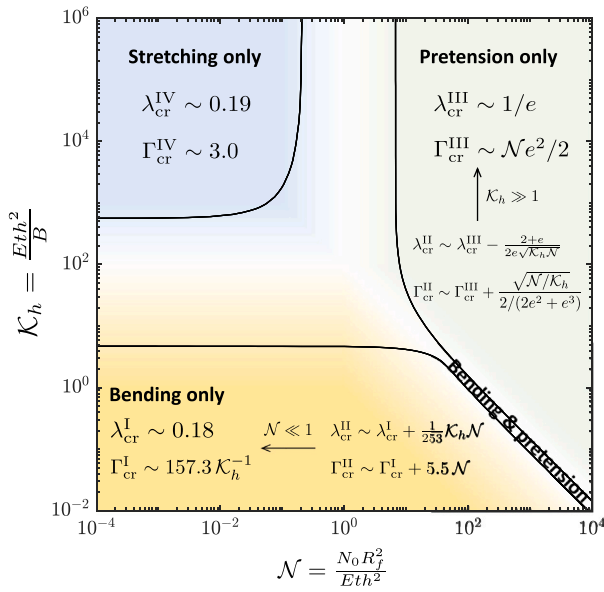


**Fig. 8.** A regime diagram for axisymmetric stiction problem. In different  $(\mathcal{K}_h, \mathcal{N})$  space, different critical adhesion energy  $\Gamma_{cr}$  is required to make the stiction happen with a minimum adhesion length  $\lambda_{cr}$ . The definition of key parameters including  $\mathcal{K}_h, \mathcal{N}, \lambda$ , and  $\Gamma$  can be found in Eq. (2.1).

a unified regime diagram in Fig. 8. In particular, we specify the critical adhesion condition and adhesion length for the bending-only regime (approximately valid when  $\mathcal{K}_h \lesssim 1$  and  $\mathcal{K}_h \mathcal{N} \lesssim 1$ ), the pretension-only regime (approximately valid when  $\mathcal{N} \gtrsim 1$  and  $\mathcal{K}_h \mathcal{N} \gtrsim 10^4$ ), the stretching-only regime (approximately valid when  $\mathcal{N} \lesssim 0.1$  and  $\mathcal{K}_h \gtrsim 10^4$ ), and the bending and pretension regime (approximately valid as long as  $\mathcal{N} \gtrsim 1$  or  $\mathcal{K}_h \lesssim 1$ ). Note that the bending and pretension regime includes two sets of analytical results for  $\mathcal{K}_h \mathcal{N} \ll 1$  and  $\mathcal{K}_h \mathcal{N} \gg 1$ , respectively. The former can decay to that in the bending-only regime as  $\mathcal{N} \ll 1$  and the latter can decay to that in the pretension-only limit as  $\mathcal{K}_h \gg 1$ . We define the boundary of different regimes (i.e., the solid curves in Eq. (2.1)) as the deviation between the asymptotic solution and the numerical result reaches 10%. We then demonstrate in Fig. 9 how this diagram can be used for the examination of the structural reliability of thin plate devices at various scales in experiments, including graphene, tungsten disulfide, and ecoflex in wearable electronics, 2D material devices, and M/NMES devices summarized in Table 1.

The physical parameters of thin plate devices summarized in Table 1 feature either large or small  $\mathcal{K}_h$ . In Fig. 9, we thus plot the numerically

calculated master curves for the stiction criterion, which are the critical  $\mathcal{K}_h \Gamma - \mathcal{K}_h \mathcal{N}$  relation (appearing as  $\mathcal{K}_h \lesssim 1$ , Fig. 9a) and the critical  $\Gamma - \mathcal{N}$  relation (appearing as  $\mathcal{K}_h \gtrsim 10^4$ , Fig. 9b). We note that these numerical curves can be approximated well by corresponding asymptotic/perturbation solutions, i.e., Eq. a for  $\mathcal{K}_h \ll 1$  and  $\mathcal{K}_h \mathcal{N} \ll 1$ , Eq. b for  $\mathcal{K}_h \ll 1$  and  $\mathcal{K}_h \mathcal{N} \gg 1$ , Eq. (3.21) for  $\mathcal{K}_h \gg 1$  and  $\mathcal{N} \gg 1$ , and Eq. (3.40) for  $\mathcal{K}_h \gg 1$  and  $\mathcal{N} \ll 1$ . We then use red-shaded regions to indicate that stiction occurred and blue-shaded regions to indicate that stiction did not take place in the experiments. To plot these regions, we have used the adhesion energy of 0.05–0.1 J/m<sup>2</sup> for 2D material plates [35] or an adhesion energy that has been specified in the report; The pretension is estimated by assuming a residual strain less than 0.1%.

Overall the theoretical prediction agrees well with experimental observations. For example, Ma et al. [14] have examined the stability of ecoflex plates with different radii and heights for wearable electronic devices (S1–S4 in Table 1). It has been found that samples S2 and S4 could collapse, while samples S1 and S3 are robust. This behavior is consistent with the theory since dimensionless adhesion energies of S1 and S3 are below the stiction criterion (the solid curve in Fig. 9a) while those of S2 and S4 have met the criterion. Another example can be given by nanochannels covered with graphite plates of thicknesses of 52 nm (S5) and 12 nm (S6) reported in Radha et al. [42]. The relatively thin sample (S6) can satisfy the stiction criterion and is found to sag in the channels. By contrast, the relatively thick sample (S5) has a small  $\mathcal{K}_h \Gamma$  and is found to be able to maintain its structural integrity. By trial and error, Yang et al. [8] and Esfandiari et al. [44] have fabricated similar “safe” nanochannels with thicknesses of the top graphite plates of 50–70 nm. The comparison in Fig. 9 suggests that these geometrical parameters can be rationally designed via the theoretically predicted stiction criterion. More recently, Ronceray et al. [43] designed nano-switch devices with top plates of thicknesses ranging from 6 to 48 nm. Collapsed nanochannels were detected even for the thickest top plates, which also agrees with our theoretical prediction in Fig. 9a.

Fig. 9b shows experiments involving very thin plates. The stiction criterion can be illustrated by the solid curve that is numerically calculated using  $\mathcal{K}_h = 10^4$  (using larger  $\mathcal{K}_h$  gives the same result). Again, this criterion agrees well with previous experiments. For example, a large number of suspended single and bilayer graphene samples in cavities with different radii and depths have been characterized by Joseá Cartamil-Bueno et al. [13]. It is found that the stiction rate of bi-layer graphene plates on cavities with depths of 630 nm and radii of  $\lesssim 5 \mu\text{m}$  (denoted as S9) is less than 5%, while the stiction rate of single-layer graphene on cavities with depths of 285 nm and radii of  $\gtrsim 5 \mu\text{m}$  (denoted as S10) is more than 92%. Other examples showing the successful prediction of our theory include monolayer graphene plates (denoted as S7 and S8) in gas impermeability tests [10]

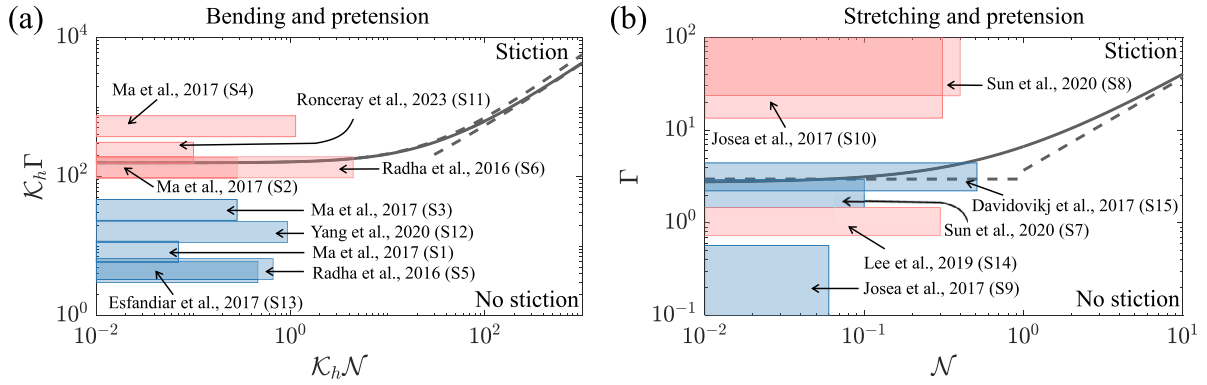


**Fig. 9.** Comparison between theoretical predictions of stiction and experimental observations in relevant wearable, 2D materials, and M/NMES devices. We use red-shaded regions to indicate that stiction is present in experiments and blue-shaded regions to indicate that the devices have been safely fabricated. (a) The stiction diagram for small  $K_h$ , i.e., that the induced stretching can be neglected. The solid curve is given by the numerical results of the critical adhesion energy for  $K_h = 10^{-1}$ . The two dashed curves represent the asymptotic solutions of bending and pretension regime as  $K_h N \ll 1$  and  $K_h N \gg 1$  (see Eq. (3.15)). (b) The stiction diagram for large  $K_h$ . The solid curve is numerically calculated for  $K_h = 10^4$  using a clamped (i.e., no-slip) boundary condition at the edge of the cavity, while the dotted line is numerically calculated using a no-shear boundary condition. Clearly, the slip of the plate on the substrate would facilitate the occurrence of stiction as it requires relatively smaller critical adhesion energies. The dashed curves are perturbation solutions obtained at the pretension-only (3.21) and stretching-only (3.40) limit.

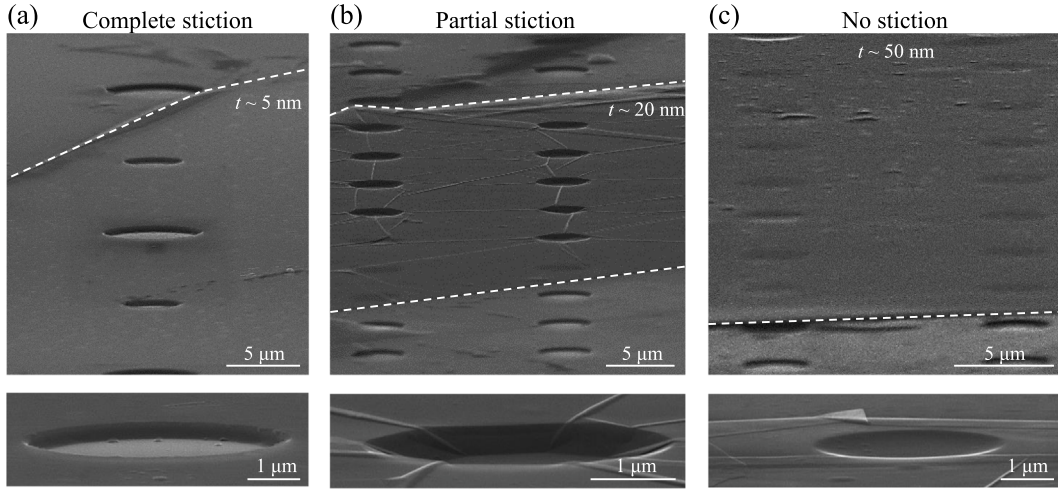


**Fig. 10.** SEM images of three typical stiction states of multilayered graphene plates on cavities: (a) Complete stiction; (b) Partial stiction; (c) No stiction. The white dashed curves denote the edge of the plate. Images in the bottom panel are zoom-in views of the graphene plate on a single cavity.

and nanomechanical graphene-based pressure sensors (S15) reported in Davidovikj et al. [11]. Note that it is not necessary for samples with dimensionless parameters lying within the stiction region to collapse since a mechanical stimulus is usually needed to initiate the stiction. Alternatively, for samples with dimensionless parameters lying within the no-stiction region, there are no reasons for them to show stiction. In this sense, the resonant pressure sensor (S14) made by Lee et al. [12] is an exception that contradicts our theory (Fig. 9b). Specifically, its dimensionless parameter is within the no-stiction region while the functional graphene plate was observed to collapse into the cavity after about two months of operation in ambient conditions [12]. One possible explanation is the slippage of the graphene plate on the substrate — this would modify the boundary condition at the edge of the cavity from no slip (in the previous discussion) to no shear (see Appendix B), which eventually turns down the stiction criterion (see the dotted curve in Fig. 9).

#### 4.2. The unexpected stiction

In order to further verify our theoretical prediction for the stiction criterion, we carry out experiments containing different 2D materials (graphene, hBN, and  $\text{MoS}_2$ ) of various thicknesses. The experiment setup is presented in Appendix D. Table 2 summarizes the key parameters

of the systems in our experiments, together with the stiction rate characterized by SEM observations. For samples whose dimensionless parameters lie in the bending-only or stretching-only regimes, we can directly use the asymptotic/perturbation solutions for the critical adhesion to predict whether stiction could occur. For samples whose dimensionless parameters indicate that both bending and stretching effects are important, we can solve the problem specified in Eqs. (2.12)–(2.15) numerically for a prediction of the stiction state. In fact, the thickness of 2D materials and the geometry of cavities used in our experiments have been designed with the aid of our theory to be capable of suppressing any stiction. Although there are three batches of samples (B2, B3, and B18) showing complete or partial stiction, most batches of samples show zero stiction rate (Table 2), which agrees well with predictions based on numerical and analytical results in Section 2 and Section 3.

Finally, we discuss possible reasons for unsuccessful predictions of our theory for B2, B3, and B18, which are supposed to show zero stiction rates. One is the slip of the material on its supporting substrate, as we have considered for the sample in Lee et al. [12]. The slip would reduce the deflection resistance of the material and thus make the occurrence of stiction more readily. This can be seen in Fig. 9b, where the dotted curve considering the slip effect shows a lower

**Table 2**

Summary of experimental results. The residual strain used to estimate the pretension is assumed to be less than 0.1% here. Stiction rate denotes the rate of samples adhered to the bottom of the cavity.

Regime		Materials	Radius $R_f$ nm	Height $h$ nm	Thickness $t$ nm	$\mathcal{K}_h$	$\mathcal{N}$	Stiction rate %
Bending – only	B1	Graphene	~1750	~300	$\geq 500$	$\leq 10^0$	$\leq 0.034$	0
Stretching – only	B2	Graphene	~2500	~300	~5	$\sim 10^4$	$\leq 0.069$	100
	B3	Graphene	~1750	~300	~5	$\sim 10^4$	$\leq 0.034$	100
	B4	Graphene	~1750	~300	~3	$\sim 10^5$	$\leq 0.034$	0
	B5	Graphene	~750	~300	~3	$\sim 10^5$	$\leq 0.006$	0
	B6	Graphene	~500	~300	~3.5	$\sim 10^5$	$\leq 0.003$	0
	B7	Graphene	~800	~300	~4	$\sim 10^5$	$\leq 0.007$	0
	B8	Graphene	~550	~300	~4.5	$\sim 10^5$	$\leq 0.003$	0
	B9	Graphene	~900	~300	~7	$\sim 10^4$	$\leq 0.009$	0
	B10	Graphene	~600	~300	~13	$\sim 10^4$	$\leq 0.004$	0
	B11	MoS <sub>2</sub>	~550	~300	~3	$\sim 10^5$	$\leq 0.003$	0
	B12	MoS <sub>2</sub>	~250	~300	~5	$\sim 10^4$	$\leq 0.001$	0
	B13	MoS <sub>2</sub>	~800	~300	~12	$\sim 10^4$	$\leq 0.007$	0
	B14	hBN	~1250	~300	~4.5	$\sim 10^4$	$\leq 0.017$	0
	B15	hBN	~500	~300	~5	$\sim 10^4$	$\leq 0.003$	0
	B16	hBN	~500	~300	~7	$\sim 10^4$	$\leq 0.003$	0
	B17	hBN	~1500	~300	~12	$\sim 10^4$	$\leq 0.025$	0
Bending & Stretching	B18	Graphene	~1750	~300	20–25	$\sim 10^3$	$\leq 0.034$	57.1
	B19	Graphene	~1750	~300	$\geq 50$	$\leq 10^2$	$\leq 0.034$	0
	B20	Graphene	~700	~300	~22	$\sim 10^3$	$\leq 0.005$	0
	B21	MoS <sub>2</sub>	~550	~300	~17	$\sim 10^3$	$\leq 0.003$	0
	B22	MoS <sub>2</sub>	~750	~300	~22	$\sim 10^3$	$\leq 0.006$	0
	B23	MoS <sub>2</sub>	~250	~300	~30	$\sim 10^3$	$\leq 0.001$	0
	B24	hBN	~1000	~300	~18	$\sim 10^3$	$\leq 0.011$	0
	B25	hBN	~1000	~300	~20	$\sim 10^3$	$\leq 0.011$	0
	B26	hBN	~1000	~300	~30	$\sim 10^3$	$\leq 0.025$	0

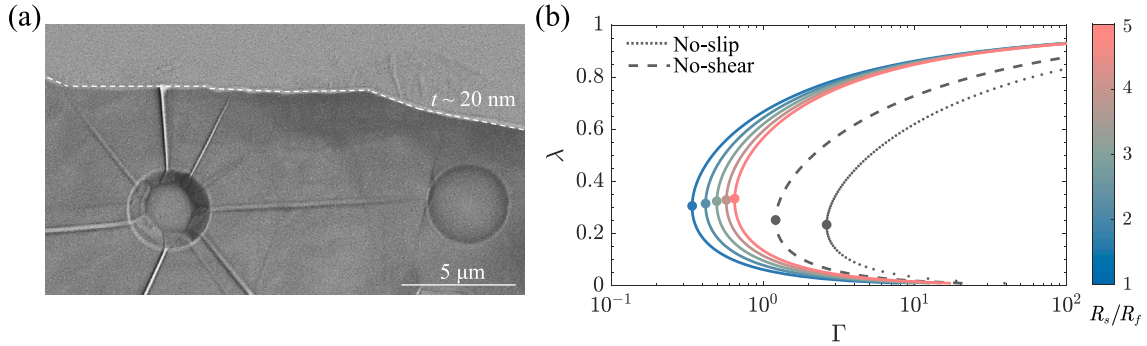


**Fig. 11.** Stiction with buckle delamination. (a) SEM image of radial buckle delamination in the supported region of a multilayer graphene plate that shows asymmetric stiction. (b) The relation between adhesion energy  $\Gamma$  and adhesion length  $\lambda$  for the plate of various physical size  $R_s$  calculated by considering the relaxation effect of buckle delamination (see details in [Appendix C](#)).

critical adhesion relative to the solid curve that used no-slip boundary conditions. The other reason for such unexpected stiction may be the buckle delamination in the substrate-supported region. As shown in [Fig. 11a](#), the plate on top of the left cavity collapses with buckle delamination while remaining suspended on top of the right cavity near which no delamination is observed. Although the buckle delamination behavior is stochastic and is not predictable by current theory, we can roughly examine how this behavior relaxes the plate and further facilitates the stiction ([Fig. 11b](#)). In particular, the colored curves are numerically calculated by considering the relaxation effect of the buckles on the hoop stress  $\mathcal{C}$ . Depending on the detailed physical size of the plate, this relaxation effect is found to reduce the critical adhesion energy (i.e., the stiction criterion) by up to an order of magnitude. However, a more formal analysis of the effect of buckle delamination is needed to take the asymmetry into account, which is beyond the scope of the present work. In addition, we have not discussed the effect of external loads such as pressure inside the cavity [34,58], the nonuniform residual stresses [59], plate-substrate shear interactions [35, 60], dynamic dissipation [61,62], and the asymmetric plate sizes on the critical adhesion length [63,64]. Controlling these factors in our

experiments is somewhat challenging at this moment, particularly due to the lack of characterization methods. Additionally, the ideal approach would be to first determine the adhesion energy through one or two experiments, and then use this value to predict whether stiction will occur. Therefore, a more comprehensive comparison with experimental measurement (e.g., specific adhesion length) would be needed to justify the analytical models presented in this work.

## 5. Conclusions

In this work, we have combined theories and experiments to clarify the physical model and key dimensionless parameters for the axisymmetric stiction problem. The focus has been on four limiting regimes (that is, the bending-only regime, the bending and pretension regime, the pretension-only regime, and the stretching-only regime) and ranges of corresponding parameters for the analyses in these regimes being applicable. As a result, we have provided a regime diagram with detailed analytical results in different parameter spaces. We have also shown that this diagram can be very useful for the design of relevant thin plate devices, particularly in avoiding the occurrence of stiction (note

that previous experiments have been much based on trial-and-error method).

The consideration of axisymmetry has allowed a set of analytical solutions to the complex stiction problem. Our numerical and analytical results have shown excellent agreement with most experimental results reported in the literature and performed in this work. However, discrepancies have been found when complex material and interface behaviors occur such as the slip and buckle delamination of the plate on the substrate. These behaviors typically play a role in reducing the resistance of the thin plate to deformations and deflections, so that the stiction could take place much more easily than the prediction of our current theory. In addition, slip and buckle delamination often breaks the axisymmetry of the system, which warrants further formal investigations to complete more accurate regime diagrams.

Though this work has focused on the stiction of plates on rigid substrates, recent experiments in flexible electronics and M/NEMNS have increasingly made use of soft substrates, raising a fundamental question regarding how substrate elasticity influences the stiction behavior [65–67]. The challenges in addressing the effect of elastic substrates include both solving the nonlinear governing equations and identifying the critical adhesion conditions [68–70]. Due to the nonlinear geometry, some analytical solutions to the problem might be obtained by approximating the displacement fields, such as the Rayleigh approximation discussed in [71]. This method has proven useful in recent studies, including Refs. [57,72–74]. However, complexities may arise in proposing appropriate simplified displacement fields for the substrate and plate in various regimes. Furthermore, the critical adhesion condition, such as Eq. (2.8), would be qualitatively modified by the deformation of the substrate. Although the problem remains solvable using Griffith fracture mechanics and JKR adhesion concepts that minimize total energy [75], it would be interesting to explore the corresponding local adhesion conditions.

#### CRedit authorship contribution statement

**Hang Li:** Writing – original draft, Software, Methodology, Investigation, Formal analysis. **Chuanli Yu:** Writing – original draft, Investigation. **Zhaohu Dai:** Writing – review & editing, Supervision, Investigation, Formal analysis, Conceptualization.

#### Declaration of competing interest

The authors declare that they have no known competing financial interests or personal relationships that could have appeared to influence the work reported in this paper.

#### Data availability

Data will be made available on request.

#### Acknowledgments

This work was financially supported by the National Natural Science Foundation of China (Grant No. 12372103 and 12302076).

#### Appendix A. Summary of previous work on the problem of axisymmetric stiction

#### Appendix B. The effect of slip boundary on the axisymmetric stiction

In Section 2, we have formulated the axisymmetric stiction problem with clamped boundary conditions (ie, no slip) at the edge of the cavity. However, for 2D material systems with slippery surfaces, the plate can slide on its supporting substrate [59,76]. Hence, this section addresses

**Table A.3**

The approach used in the reference is indicated by N (Numerical method), E (Experimental method), and/or A (Analytical method). Note that the solutions given in [31,33] are approximate since they assumed a uniform, equibiaxial stress state.

Reference	Bending	Stretching	Pretension
[31]	–	A(approx.)	–
[32]	–	A(approx.)	–
[48]	A	–	A
[49]	A	–	A
[50]	–	A(approx.)	A
[51]	–	A(approx.)	A
[34]	A&N	A&N	A
[52]	–	–	A
[26]	A	–	–
[33]	–	A(approx.)&E	–
[15]	A	–	–
[27]	A&E	–	–
[30]	E&N	E&N	–
[28]	A&N	N	–
This work	A&N&E	A&N&E	A&N&E

the other extreme, i.e., no-shear boundary conditions at the edge of the cavity, particularly its effect on the stiction criterion.

The bending energy of the system subjected to no-shear boundary conditions remains the same as Eq. (2.3a). As slip occurs, the stretching energy becomes

$$\Pi_S = 2\pi \int_0^{R_f} \left( \frac{1}{2} N_r \epsilon_r + \frac{1}{2} N_\theta \epsilon_\theta \right) r dr + 2\pi \int_{R_f}^{R_s} \left( \frac{1}{2} N_r \epsilon_r + \frac{1}{2} N_\theta \epsilon_\theta \right) r dr, \quad (\text{B.1})$$

where  $R_s$  is the physical size of the plate. As a consequence, while in-plane equilibrium equation (Eq. (2.4)) and the out-of-plane equilibrium equation (Eq. (2.5)) for  $0 < r < R_f$  are still valid, they must be solved with modified boundary conditions at  $r = R_f$ . Specifically, the solution to the in-plane equilibrium equation for  $R_f < r < R_s$  can be obtained from Lamé solution:

$$N_r = c \left( \frac{1}{r^2} - \frac{1}{R_s^2} \right) + N_0 \quad \text{and} \quad N_\theta = -c \left( \frac{1}{r^2} + \frac{1}{R_s^2} \right) + N_0, \quad (\text{B.2})$$

where  $c$  is constant. Therefore, the boundary conditions at the edge of the cavity is modified by the slip to be:

$$\frac{R_s^2 R_f^2}{R_s^2 - R_f^2} [N_r(R_f) - N_0] + \frac{R_s^2 R_f^2}{R_s^2 + R_f^2} [N_\theta(R_f) - N_0] = 0. \quad (\text{B.3})$$

Clearly, the detailed effect of slip boundary conditions on the stiction criterion depends on the physical size of the plate  $R_s$ . For the dotted curve shown in Fig. 9b, we adopted an infinitely large size (i.e.,  $R_s \rightarrow \infty$ ) so that Eq. (B.3) becomes

$$N_r(R_f) + N_\theta(R_f) - 2N_0 = 0. \quad (\text{B.4})$$

Notably, the adhesion condition given in Eq. (2.8) is not affected by the slip.

At the stretching-only limit, the modified boundary condition at  $r = R_f$  also changes coefficients in the perturbation solution. Particularly, we find the integration constants in Eqs. (3.34) and (3.35) become Poisson's ratio independent:

$$d_1 = -\frac{8 + \lambda^2}{4(16 - \lambda^{10/3})}, \quad \text{and} \quad d_2 = -\frac{2\lambda^2 + \lambda^{10/3}}{2(16 - \lambda^{10/3})}. \quad (\text{B.5})$$

The perturbation solution for the axisymmetric stiction with slip boundary conditions and corresponding numerical results are provided in Fig. B.12. In this case, the error of the perturbation solution is enlarged because the error of the original base solution in Eq. (3.29) is not small anymore and the leading-order correction becomes insufficient.



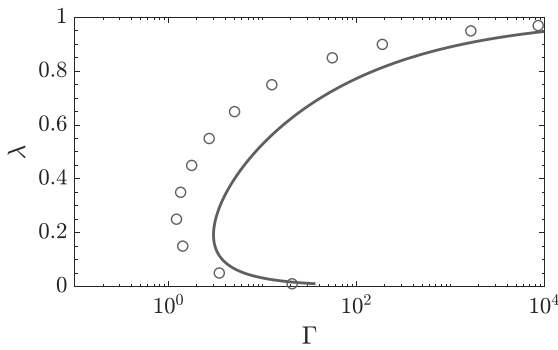


**Fig. B.12.** Comparison between the numerical solution and the perturbation solution for the axisymmetric stiction with slip boundary conditions. The solid curve denotes the perturbation solution (3.34) with updated coefficients given in Eq. (B.5). The markers represent the corresponding numerical results obtained from the un-simplified model (2.12)–(2.15) using  $\mathcal{K}_h = 10^4$  and  $\mathcal{N} = 0$  and replaced slip boundary condition at the edge of the cavity, i.e., Eq. (B.4).

### Appendix C. The effect of buckle delamination on the stiction criterion

We roughly consider how the occurrence of buckle delamination modifies the axisymmetric stiction problem. First, this has to do with the slip of the plate on the substrate (as discussed in Appendix B). Secondly, the buckles would relax the hoop stress in the substrate-supported plate to be

$$N_\theta = -\frac{2B}{\mu^2}, \quad (\text{C.1})$$

where  $\mu$  is the wavelength of the buckle [59,77]. As a result, the in-plane equilibrium equation for  $R_f < r < R_s$  should be rewritten as

$$\frac{d}{dr} (rN_r) + \frac{2B}{\mu^2} = 0. \quad (\text{C.2})$$

To solve the colored curves in Fig. 11b, we have focused on the stretching-only limit where we used  $N_r(R_s) = 0$  and  $\mathcal{K}_h = 10^4$ . According to Eq. (C.2), we then set the radial stress at the edge of the cavity to be

$$N_r = \frac{2B}{\mu^2} \left( \frac{R_s}{R_f} - 1 \right), \quad (\text{C.3})$$

which is in contrast to the boundary condition (B.4) that considers the slip effect but neglects the relaxation effect by the buckle delamination. Note that this is a rather simplified treatment (more formal analysis may need to consider the asymmetric geometry of the stiction and the far-field behavior of the plate in the substrate-supported region).

### Appendix D. Experimental setup

In order to further verify our theoretical prediction for the stiction criterion, we perform experiments containing different 2D materials (graphene, hBN, and MoS<sub>2</sub>) of various thicknesses. Briefly, these 2D material plates are mechanically exfoliated onto silica/silicon substrates that are prepatterned with an array of circular cavities with depths of approximately 300 nm and diameters ranging from 250 to 5000 nm. The 2D material/substrate assemblies are then placed in SEM chamber for the direct observation of stiction. Note that during the vacuuming process, the suspended 2D material plates could be mechanically disturbed to make contact with the bottom of the cavity, as illustrated in Fig. D.13. Next, we used SEM and AFM to characterize the stiction state of 2D materials. Fig. 10 shows typical stiction states of graphene plates on an array of cavities, including complete stiction, partial stiction, and no stiction. We then use AFM to determine the thickness of these 2D

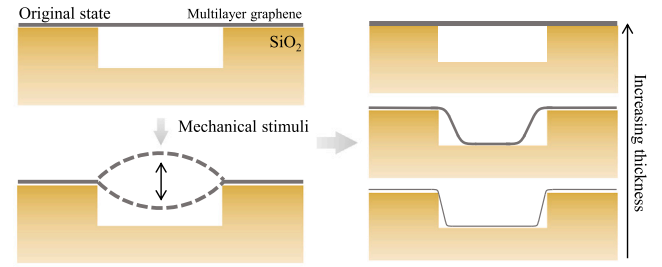


**Fig. D.13.** Schematic illustration of the experimental set-up in which 2D materials are transferred on top of the cavity. Mechanical stimuli are applied by the vacuuming operation to make possible contact between the plate and the bottom of the cavity.

material plates as well as the geometry of the cavities, giving rise to the key parameters of the system as summarized in Table 2.

### References

- [1] Freund LB, Suresh S. Thin film materials: stress, defect formation and surface evolution. Cambridge University Press; 2004.
- [2] Bico J, Reyssat É, Roman B. Elastocapillarity: When surface tension deforms elastic solids. Annu Rev Fluid Mech 2018;50:629–59. <http://dx.doi.org/10.1146/annurev-fluid-122316-050130>.
- [3] Smith A, Niklaus F, Paussa A, Vaziri S, Fischer AC, Sterner M, et al. Electromechanical piezoresistive sensing in suspended graphene membranes. Nano Lett 2013;13(7):3237–42. <http://dx.doi.org/10.1021/nl401352k>.
- [4] Dolleman RJ, Davidovikj D, Cartamil-Bueno SJ, van der Zant HS, Steeneken PG. Graphene squeeze-film pressure sensors. Nano Lett 2016;16(1):568–71. <http://dx.doi.org/10.1021/acs.nanolett.5b04251>.
- [5] Smith AD, Niklaus F, Paussa A, Schröder S, Fischer AC, Sterner M, et al. Piezoresistive properties of suspended graphene membranes under uniaxial and biaxial strain in nanoelectromechanical pressure sensors. ACS Nano 2016;10(11):9879–86. <http://dx.doi.org/10.1021/acs.nano.6b02533>.
- [6] Sulleiro MV, Dominguez-Alfaro A, Alegret N, Silvestri A, Gómez IJ. 2D materials towards sensing technology: From fundamentals to applications. Sensing Bio-Sens Res 2022;100540. <http://dx.doi.org/10.1016/j.sbsr.2022.100540>.
- [7] Chen Y, Lu D, Kong L, Tao Q, Ma L, Liu L, et al. Mobility enhancement of strained MoS<sub>2</sub> transistor on flat substrate. ACS Nano 2023;17(15):14954–62. <http://dx.doi.org/10.1021/acs.nano.3c03626>.
- [8] Yang Q, Sun P, Fumagalli L, Stebunov Y, Haigh S, Zhou Z, et al. Capillary condensation under atomic-scale confinement. Nature 2020;588(7837):250–3. <http://dx.doi.org/10.1038/s41586-020-2978-1>.
- [9] Zhao Y, Wang L, Yu T. Mechanics of adhesion in MEMS-a review. J Adhes Sci Technol 2003;17(4):519–46. <http://dx.doi.org/10.1163/15685610360554393>.
- [10] Sun P, Yang Q, Kuang W, Stebunov Y, Xiong W, Yu J, et al. Limits on gas impermeability of graphene. Nature 2020;579(7798):229–32. <http://dx.doi.org/10.1038/s41586-020-2070-x>.
- [11] Davidovikj D, Scheepers PH, van der Zant HS, Steeneken PG. Static capacitive pressure sensing using a single graphene drum. ACS Appl Mater Interfaces 2017;9(49):43205–10. <http://dx.doi.org/10.1021/acsami.7b17487>.
- [12] Lee M, Davidovikj D, Sajadi B, Šiškins M, Alijani F, van der Zant HS, et al. Sealing graphene nanodrums. Nano Lett 2019;19(8):5313–8. <http://dx.doi.org/10.1021/acs.nanolett.9b01770>.
- [13] José Cartamil-Bueno S, Centeno A, Zurutuza A, Gerard Steeneken P, der Zant HSJ, Houris S. Very large scale characterization of graphene mechanical devices using a colorimetry technique. Nanoscale 2017;9(22):7559–64. <http://dx.doi.org/10.1039/C7NR01766A>.
- [14] Ma Y, Pharr M, Wang L, Kim J, Liu Y, Xue Y, et al. Soft elastomers with ionic liquid-filled cavities as strain isolating substrates for wearable electronics. Small 2017;13(9):1602954. <http://dx.doi.org/10.1002/sml.201602954>.
- [15] Wang X, Ma Y, Xue Y, Luan H, Pharr M, Feng X, et al. Collapse of liquid-overfilled strain-isolation substrates in wearable electronics. Int J Solids Struct 2017;117:137–42. <http://dx.doi.org/10.1016/j.ijsolstr.2017.03.031>.
- [16] Dai Z, Liu L, Zhang Z. Strain engineering of 2D materials: issues and opportunities at the interface. Adv Mater 2019;31(45):1805417. <http://dx.doi.org/10.1002/adma.201805417>.
- [17] Meng G, Ko WH. Modeling of circular diaphragm and spreadsheet solution programming for touch mode capacitive sensors. Sensors Actuators A 1999;75(1):45–52. [http://dx.doi.org/10.1016/S0924-4247\(99\)00055-2](http://dx.doi.org/10.1016/S0924-4247(99)00055-2).
- [18] Fragiaco G, Ansbæk T, Pedersen T, Hansen O, Thomsen EV. Analysis of small deflection touch mode behavior in capacitive pressure sensors. Sensors Actuators A 2010;161(1–2):114–9. <http://dx.doi.org/10.1016/j.sna.2010.04.030>.



- [19] Kang M-C, Rim C-S, Pak Y-T, Kim W-M. A simple analysis to improve linearity of touch mode capacitive pressure sensor by modifying shape of fixed electrode. *Sensors Actuators A* 2017;263:300–4. <http://dx.doi.org/10.1016/j.sna.2017.06.024>.
- [20] Chun S, Kim Y, Oh H-S, Bae G, Park W. A highly sensitive pressure sensor using a double-layered graphene structure for tactile sensing. *Nanoscale* 2015;7(27):11652–9. <http://dx.doi.org/10.1039/C5NR00076A>.
- [21] Berger C, Phillips R, Centeno A, Zurutuza A, Vijayaraghavan A. Capacitive pressure sensing with suspended graphene–polymer heterostructure membranes. *Nanoscale* 2017;9(44):17439–49. <http://dx.doi.org/10.1039/C7NR04621A>.
- [22] Gupta A, Ahmad A, Singh R. Capacitive pressure sensor for MEMS. In: *Smart Mater Struct Syst*. 5062, SPIE; 2003, p. 450–4. <http://dx.doi.org/10.1117/12.514570>.
- [23] Johnson KL, Johnson KL. *Contact mechanics*. Cambridge University Press; 1987.
- [24] Mansfield EH. *The bending and stretching of plates*. Cambridge University Press; 2005.
- [25] Audoly B, Pomeau Y. *Elasticity and geometry*. Oxford University Press; 2010.
- [26] Liu J. Theoretical analysis on capillary adhesion of micro-sized plates with a substrate. *Acta Mech Sinica* 2010;26(2):217–23. <http://dx.doi.org/10.1007/s10409-009-0318-7>.
- [27] Xue Y, Kang D, Ma Y, Feng X, Rogers JA, Huang Y. Collapse of microfluidic channels/reservoirs in thin, soft epidermal devices. *Extreme Mech Lett* 2017;11:18–23. <http://dx.doi.org/10.1016/j.eml.2016.11.012>.
- [28] Sun Y, Wang X, Guo X, Mei Y. Adhesion behavior of an extensible soft thin film-substrate system based on finite deformation theory. *Eur J Mech A Solids* 2021;85:104115. <http://dx.doi.org/10.1016/j.euromechsol.2020.104115>.
- [29] Chandler TG, Vella D. Indentation of suspended two-dimensional solids: The signatures of geometrical and material nonlinearity. *J Mech Phys Solids* 2020;144:104109. <http://dx.doi.org/10.1016/j.jmps.2020.104109>.
- [30] Gong Y, Mei Y, Liu J. Capillary adhesion of a circular plate to solid: Large deformation and movable boundary condition. *Int J Mech Sci* 2017;126:222–8. <http://dx.doi.org/10.1016/j.ijmecsci.2017.03.030>.
- [31] Williams J. Energy release rates for the peeling of flexible membranes and the analysis of blister tests. *Int J Fract* 1997;87:265–88. <http://dx.doi.org/10.1023/A:1007314720152>.
- [32] Wan K-T. Adherence of an axisymmetric flat punch on a thin flexible membrane. *J Adhes* 2001;75(4):369–80. <http://dx.doi.org/10.1080/00218460108029611>.
- [33] Xu D, Liechti KM. Analytical and experimental study of a circular membrane in adhesive contact with a rigid substrate. *Int J Solids Struct* 2011;48(20):2965–76. <http://dx.doi.org/10.1016/j.ijsolstr.2011.06.014>.
- [34] Jin C. Theoretical study of mechanical behavior of thin circular film adhered to a flat punch. *Int J Mech Sci* 2009;51(6):481–9. <http://dx.doi.org/10.1016/j.ijmecsci.2009.04.003>.
- [35] Dai Z, Lu N, Liechti KM, Huang R. Mechanics at the interfaces of 2D materials: Challenges and opportunities. *Curr Opin Solid State Mater Sci* 2020;24(4):100837. <http://dx.doi.org/10.1016/j.cossms.2020.100837>.
- [36] Wang G, Dai Z, Xiao J, Feng S, Weng C, Liu L, et al. Bending of multilayer van der Waals materials. *Phys Rev Lett* 2019;123(11):116101. <http://dx.doi.org/10.1103/PhysRevLett.123.116101>.
- [37] Vel SS, Maalouf SR. Bending and twisting rigidities of 2D materials. *Int J Mech Sci* 2024;109501.
- [38] Shen X, Wei Y, Liu Y. Unlocking slip-mediated bending in multilayers: Efficient modeling and solutions with high precision and simplicity. *Int J Solids Struct* 2024;112971.
- [39] Johnson K, Greenwood J. An adhesion map for the contact of elastic spheres. *J Colloid Interface Sci* 1997;192(2):326–33. <http://dx.doi.org/10.1006/jcis.1997.4984>.
- [40] Yu C, Dai Z. Characterizing the wetting behavior of 2D materials: a review. *J Mater Inf* 2023;3(3):20.
- [41] Rao Y, Kim E, Dai Z, He J, Li Y, Lu N. Size-dependent shape characteristics of 2D crystal blisters. *J Mech Phys Solids* 2023;175:105286. <http://dx.doi.org/10.1016/j.jmps.2023.105286>.
- [42] Radha B, Esfandiar A, Wang F, Rooney A, Gopinadhan K, Keerthi A, et al. Molecular transport through capillaries made with atomic-scale precision. *Nature* 2016;538(7624):222–5. <http://dx.doi.org/10.1038/nature19363>.
- [43] Ronceray N, Spina M, Chou VHY, Lim CT, Geim AK, Garaj S. Programmable 2D nano-switches and nano-capsules enclosing zeptoliter liquid volumes. 2023. <http://dx.doi.org/10.48550/arXiv.2311.08748>, arXiv preprint arXiv:2311.08748.
- [44] Esfandiar A, Radha B, Wang F, Yang Q, Hu S, Garaj S, et al. Size effect in ion transport through angstrom-scale slits. *Science* 2017;358(6362):511–3. <http://dx.doi.org/10.1126/science.adc9931>.
- [45] Majidi C, Adams GG. A simplified formulation of adhesion problems with elastic plates. *Proc Royal Soc A: Math Phys Eng Sci* 2009;465(2107):2217–30. <http://dx.doi.org/10.1098/rspa.2009.0060>.
- [46] Glassmaker N, Hui C. Elastic solution for a nanotube formed by self-adhesion of a folded thin film. *J Appl Phys* 2004;96(6):3429–34. <http://dx.doi.org/10.1063/1.1779974>.
- [47] Py C, Reverdy P, Doppler L, Bico J, Roman B, Baroud CN. Capillary origami: spontaneous wrapping of a droplet with an elastic sheet. *Phys Rev Lett* 2007;98(15):156103. <http://dx.doi.org/10.1103/PhysRevLett.98.156103>.
- [48] Wan K-T. Adherence of an axisymmetric flat punch onto a clamped circular plate: transition from a rigid plate to a flexible membrane. *J Appl Mech* 2002;69(2):110–6. <http://dx.doi.org/10.1115/1.1433477>.
- [49] Wong M-F, Duan G, Wan K-T. Adhesion–delamination mechanics of a prestressed circular film adhered onto a rigid substrate. *J Adhes* 2007;83(1):67–83. <http://dx.doi.org/10.1080/00218460601102878>.
- [50] Wan K-T, Dillard DA. Adhesion of a flat punch adhered to a thin prestressed membrane. *J Adhes* 2003;79(2):123–40. <http://dx.doi.org/10.1080/00218460309573>.
- [51] Wan K-T, Kogut L. The coupling effect of interfacial adhesion and tensile residual stress on a thin membrane adhered to a flat punch. *J Micromech Microeng* 2005;15(4):778. <http://dx.doi.org/10.1088/0960-1317/15/4/015>.
- [52] Wang S, Li X. The coupling effect of punch shape and residual stress on measuring adhesion work of membrane by pull-off test. *Thin Solid Films* 2010;518(21):6036–9. <http://dx.doi.org/10.1016/j.tsf.2010.06.021>.
- [53] Li G, Wan K-T. Adhesion map for thin membranes. *J Appl Mech* 2014;81(2):021018. <http://dx.doi.org/10.1115/1.4025303>.
- [54] Zhu T, Li G, Müftü S, Wan K-T. Revisiting the constrained blister test to measure thin film adhesion. *J Appl Mech* 2017;84(7):071005. <http://dx.doi.org/10.1115/1.4036776>.
- [55] Schwerin E. Über spannungen und formänderungen kreisringförmiger membran. *Z Ang Math Mech* 1929;9(6):482–3. <http://dx.doi.org/10.1002/zamm.19290090609>.
- [56] Vella D, Davidovitch B. Indentation metrology of clamped, ultra-thin elastic sheets. *Soft Matter* 2017;13(11):2264–78. <http://dx.doi.org/10.1039/C6SM02451C>.
- [57] Chen E, Dai Z. Axisymmetric peeling of thin elastic films: A perturbation solution. *J Appl Mech* 2023;90(10):1–15. <http://dx.doi.org/10.1115/1.4062831>.
- [58] Plaut RH. Effect of pressure on pull-off of flat 1-D rectangular punch adhered to membrane. *J Adhes* 2022;98(10):1480–500. <http://dx.doi.org/10.1080/00218464.2021.1908140>.
- [59] Dai Z, Sanchez DA, Brennan CJ, Lu N. Radial buckle delamination around 2D material tents. *J Mech Phys Solids* 2020;137:103843. <http://dx.doi.org/10.1016/j.jmps.2019.103843>.
- [60] Cong C, Wei Y, Wei X. Trans-scale dynamic shear-lag model for wave attenuation in staggered composites. *Int J Mech Sci* 2023;238:107841.
- [61] Ciavarella M, Zhang T, McMeeking RM. External work rate and dissipation during crack growth in a viscoelastic material. *J Mech Phys Solids* 2022;169:105096.
- [62] Ceglie M, Menga N, Carbone G. Modelling the non-steady peeling of viscoelastic tapes. *Int J Mech Sci* 2024;267:108982.
- [63] Sanchez DA, Dai Z, Wang P, Cantu-Chavez A, Brennan CJ, Huang R, et al. Mechanics of spontaneously formed nanoblister trapped by transferred 2D crystals. *Proc Natl Acad Sci* 2018;115(31):7884–9.
- [64] Fang Z, Dai Z, Wang B, Tian Z, Yu C, Chen Q, et al. Pull-to-peel of two-dimensional materials for the simultaneous determination of elasticity and adhesion. *Nano Lett* 2022;23(2):742–9.
- [65] Skotheim J, Mahadevan L. Soft lubrication. *Phys Rev Lett* 2004;92(24):245509. <http://dx.doi.org/10.1103/PhysRevLett.92.245509>.
- [66] Sun Y, Chen R, Wang W, Zhang J, Qiu W, Liu X, et al. Rate-dependent pattern evolution in peeling adhesive tape driven by cohesive failure. *Langmuir* 2022;38(42):12785–94. <http://dx.doi.org/10.1021/acs.langmuir.2c01427>.
- [67] Cai Y, Qu S, Jia Z. Anomalous fracture behavior of soft layered materials. *Int J Mech Sci* 2024;267:109018.
- [68] Perrin H, Eddi A, Karpitschka S, Snoeijer JH, Andreotti B. Peeling an elastic film from a soft viscoelastic adhesive: experiments and scaling laws. *Soft Matter* 2019;15(4):770–8. <http://dx.doi.org/10.1039/C8SM01946K>.
- [69] Zhu Y, Zheng Z, Huang C, Yu J. An analytical self-consistent model for the adhesion of gibson solid. *Int J Mech Sci* 2023;249:108246. <http://dx.doi.org/10.1016/j.ijmecsci.2023.108246>.
- [70] Yu C, Cao J, Zhu S, Dai Z. Preparation and modeling of graphene bubbles to obtain strain-induced pseudomagnetic fields. *Materials* 2024;17(12):2889.
- [71] Ciavarella M, Barber J. Indentation of a stiff membrane on an incompressible elastic halfspace. 2024, Preprint, <https://www.researchgate.net/publication/380186627>.
- [72] Afferrante L, Carbone G, Demelio G, Pugno N. Adhesion of elastic thin films: Double peeling of tapes versus axisymmetric peeling of membranes. *Tribol Lett* 2013;52:439–47.
- [73] Dai Z. Analytical solutions for circular elastic membranes under pressure. *J Appl Mech* 2024;91(8):081002.
- [74] Cao G, An F. An innovative approach to characterize the elastic moduli of 2d materials from the central strain of bulged membrane. *Int J Mech Sci* 2024;274:109254.
- [75] Ciavarella M, Joe J, Papangelo A, Barber J. The role of adhesion in contact mechanics. *J R Soc Interface* 2019;16(151):20180738.
- [76] Dai Z, Lu N. Poking and bulging of suspended thin sheets: Slippage, instabilities, and metrology. *J Mech Phys Solids* 2021;149:104320. <http://dx.doi.org/10.1016/j.jmps.2021.104320>.
- [77] Box F, Domino L, Corvo TO, Adda-Bedia M, Démery V, Vella D, et al. Delamination from an adhesive sphere: Curvature-induced dewetting versus buckling. *Proc Natl Acad Sci* 2023;120(12):e2212290120. <http://dx.doi.org/10.1073/pnas.2212290120>.